Arabian Journal for Science and Engineering (2024) 49:577–598
https://doi.org/10.1007/s13369-023-08271-0

RESEARCH ARTICLE-CHEMISTRY

Simple, Low-Priced, of Single-Step, and Fast Method for Fabricating and Immobilizing a Commercially Viable Catalyst for the Removal of Azo-Dyes from Water

Hassan E. M. Gomaa[1,2,4] · Fatma A. Gomaa[1,3] · Abdullah A. Alotaibi[1,4]

Received: 9 June 2023 / Accepted: 28 August 2023 / Published online: 28 September 2023

Abstract
This work aimed to develop and optimize a simple and rapid method to fabricate a commercially viable catalyst for treating colored, organics-pregnant wastewater effluents for small and medium units requiring simplified fixed installations and medium-skilled labor. This work concentrated on the direct immobilization of CuO onto quartz sand. The crystallography features confirmed complete crystallization in the Tenorite phase. Tenorite grain size showed propagation with annealing temperatures (AT) and slower cooling rates (CR). The SEM confirmed their uniform spherical particles in the submicron range (400–600 nm). A thorough statistical analysis was conducted to infer the optimum synthesis conditions: AT ≈ 400 °C and CR: SC. The fabricated material has demonstrated promising and superior catalytic activity performance for removing organic pollutants. The dynamic optimization plot helped infer the optimum conditions yielding the highest % decolorizing, > 95%, as 0.5 g of 5400Aq catalyst, ≈ 2.0 mL of 3% H_2O_2, and pH: 2. The dye decays exponentially according to pseudo-first-order kinetics with a half-life time of 3.7 min in case of 5400Aq. The results suggest that the fabricated CuO-coated sand is an effective and commercially viable catalyst, simple, cost-effective, reliable, readily applicable and separable, efficient, enhanced process kinetic, and needs no irradiation.

Keywords AOPs · Copper oxide · Quartz sand · Immobilization · Catalyst fabrication · Contaminants removal

1 Introduction

Pollution of water bodies can be defined as the reach of contaminants without adequate treatment into them, causing environmental harm and affecting the entire biosphere. Adequate treatments mean eliminating the potentially toxic compounds (PTCs) or transforming the malignant forms into benign ones. United Nations (UN) stated in UN Decade for Water 2005–2015 focus area entitled water and sustainable development: "Water is at the core of sustainable development and is critical for socio-economic development, healthy ecosystems, and human survival. It is vital for reducing the global disease burden and improving populations' health, welfare, and productivity." [1]. Population growth, industrial and agriculture expansion, regional imbalances, urbanization, and higher living standards will continue to increase global water demand [2] and adversely impact the water and environment by the concomitantly increased discharges, effluents, and urban emissions [3]. Accordingly, environmental protection agencies and public health organizations

✉ Hassan E. M. Gomaa
hjomaah@su.edu.sa; hassan_emgh@yahoo.com

✉ Abdullah A. Alotaibi
aaalotaibi@su.edu.sa

Fatma A. Gomaa
fjomaah@su.edu.sa

[1] Department of Chemistry, College of Science and Humanities, Shaqra University, 11911 Ad-Dawadmi, Saudi Arabia

[2] Department of Nuclear Safety Engineering, Nuclear Installations Safety Division, Atomic Energy Authority, Nasr City, Cairo 11765, Egypt

[3] Department of Chemistry, College of Women for Science, Arts, and Education, Ain Shams University, Cairo 11757, Egypt

[4] Water Research Group, College of Science and Humanities at Ad-Dawadmi, Shaqra University, 11911 Ad-Dawadmi, Saudi Arabia

worldwide issued quality standards for wastewater effluents and industrial discharges to control and prevent water resources pollution and protect the aquatic environment, habitats, and biodiversity. The world health organization (WHO) guidelines for drinking water quality provide the framework for public health protection and risk management recommendations. Under the Safe Drinking Water Act (SDWA) of 1996, the U.S. EPA enforces the national primary drinking water regulations for 91 contaminants, including microorganisms, disinfectants, disinfection byproducts, radionuclides, and other inorganic and organic compounds. The 1996 SDWA Amendments set the process for further contaminant regulations and standard-setting through Contaminant Candidate Lists (CCLs) and subsequent Regulatory Determinations (RDs). Over 100 organic and inorganic compounds are currently listed on the latest CCL (CCL4) to be considered for regulation upon RDs [2, 4]. These water regulations will continue driving the implementation of wastewater treatment processes.

Synthetic organic dyes are utilized in wide-spectrum industries such as paper, textile dyeing, cosmetic ingredients, pharmaceuticals, and many other sectors [5]. The uncontrolled release of untreated textile and dye-house effluents may cause serious consequences such as abnormal coloration of the water bodies, eutrophication, and poor water quality, directly affecting the aquatic fauna and flora and threatening environmental safety [6, 7]. Ten thousand types of textile dyes were reported to be regularly used in different industrial sectors in amounts of about 280,000 tons per year, of which 15–50% are discharged as industrial effluents worldwide every year. 70% of the total textile dyestuffs are azo dyes [8, 9], which involves cleavage of the azo bond during their photocatalytic degradation generating mutagenic and carcinogenic aromatic amines [10, 11] necessitating efficient treatment methods with no problematic secondary products. Researchers have reported and continue to develop various treatment methods such as ozonation [12], adsorption [13, 14], ion exchange and membrane processes [15], biological methods [8, 11, 16], and oxidative methods [17–22]. Dyes in wastewater severely affect the nature and quality of water by inhibiting sunlight penetration into the stream, thereby reducing the photosynthesis reaction [23].

Numerous studies demonstrated and continued to climb the elimination of organic pollutants by oxidative methods due to the ability to completely decompose the pollutant into CO_2 and H_2O end products [2, 3]. These processes are collectively termed advanced oxidation processes (AOPs), deserve the researchers' interest, and utilize heterogeneous catalysis to generate in situ reactive oxidative species (ROSs) to attack pollutants cleaving their linkage bonds. The AOPs were defined by Glaze et al. [24] as: "near ambient temperature and pressure water treatment processes which involve the generation of hydroxyl radicals in sufficient quantity to effect water purification". Afterward, the international union of pure and applied chemistry (IUPAC) stated that "advanced oxidation technologies (AOTs), which involve the in situ generations of highly potent chemical oxidants, such as the hydroxyl radical (·OH), have emerged as an important class of technologies for accelerating the oxidation (and hence removal) of a wide range of organic contaminants in polluted water and air." [25]. AOTs involve various activation and oxidants generation methods and may utilize several mechanisms for organic contaminant removal, sharing the common denominator of hydroxyl radical chemistry [25]. The central requirement of efficient AOPs is the fast generation of ROSs in adequate amounts, a function of the employed catalyst, among other experimental conditions. The catalyst is usually a semiconductor powder (mostly metal oxides) that is, if photo-induced requires UV–Vis irradiation to produce ROSs such as hydroxyl (·OH) or superoxide radicals ($\cdot O_2^-$), able to completely degrade various organic compounds without forming secondary hazardous byproducts [5, 15, 26–33].

Heterogeneous catalysts gained significant attractiveness affording high reactivity for ROSs generation in addition to their thermal stability, separability, and reusability [34, 35]. Titanium dioxide (TiO_2) is the most common efficient catalyst for the oxidation of various compounds, provided that it is activated by UV irradiation [21, 36–38]. Due to the practical complications and higher energy consumption of UV irradiation-based systems and higher cost of TiO_2, other semiconductors metal oxides have been tested, such as zinc oxide (ZnO) [39, 40], nickel oxide (NiO) [41–43], ferrite (Fe_2O_3) [39, 44], and cadmium sulfide (CdS) [45, 46]. Due to its inherent features, such as high activity, excellent electrical, physical, and magnetic properties [47], affording a narrow band gap of 1.2–1.5 eV [48], and low cost, copper oxide has attracted considerable interest and widely researched in the last 30 years. The use of CuO in free form with hydrogen peroxide and persulfate as oxidants showed promising performance features, demonstrating that the reaction is not Fenton-like [5, 49–52].

However, few AOPs are implemented worldwide due to some practical challenges and aspects which should be studied, addressed, and resolved to increase the benefits and reduce the shortcomings' cost. High-cost, electrical energy consumption, efficient catalysts fabrication, effective catalyst separation and reuse methods restricted operating conditions, catalyst debris and leachate separation, need for effluents chemistry re-modification before discharging to the sewer system or environment, and equipment requirements are among such challenges. Efficient catalyst materials fabrication has great room for enhancing the whole process performance, especially separability, and reducing the agglomeration tendency from the practical point of view. Hence, it is urgent to look for solutions and procedures to overcome and/or minimize such challenges and improve

performance and the economy. Immobilizing catalysts on a suitable support or carrier may provide a practical solution for agglomeration and separability problems.

Immobilization of catalysts in a way to maintain their catalytic properties is a must for large-scale use to enhance the reaction further and pick up heterogeneous catalysis merits. Various applications could benefit from such enhancements and immobilizations, such as effluents' contaminant degradation, alternative energy, and chemical processes [53]. Many supporters have been tested, including alumina [54], silica [55, 56], polymers [35], zeolites [57], and sand [53, 58]. The catalytic features of immobilized or anchored catalysts to different types of supporters were studied extensively [59–63]. CuO immobilization was also investigated [3, 41, 53, 55, 58]. Various kinds of supporters have been proposed and investigated, such as alumina [41, 54], zeolite [64, 65], activated carbon [61, 66, 67], clay and montmorillonite [3, 58], and sand [53, 55, 58, 68]. Also, different immobilization or incorporation methods have been devised, proving success and usefulness with different degrees from the catalytic performance point of view, such as wet impregnation-calcination, sonication, deposition, chemical, and physical vapor deposition [53, 55, 60, 69–72].

The ideal support is the one that enhances the catalytic performance of the catalyst, provides a ground for uniform and homogenous distribution of the catalyst, is available in large amounts with low prices, is inert to the reaction mixture, or is taking part in the reaction in the right way as that of the catalyst, mechanically fit, easily separable with contaminating the reaction mixture, and eco-friendly. Moreover, the immobilization method should be easy, fast, require no fixed or complicated installations or preparation steps, low-priced, requires reasonable time scales for completion, and suitable for massive production, and easily scalable to the industrial level.

Complete degradation of a contaminant's simulant within short periods (enhanced process kinetic), low peroxide concentration, lower temperature, without UV light, moderate pH ranges, and enhanced catalyst durability are the main optimization parameters to achieve the projected goal. Hence, it is urgent to look for solutions and procedures to overcome and/or minimize such challenges and improve performance and the economy.

So, the current work attempted to develop and optimize a simple, cost-effective, reliable, readily applicable, separable, and efficient immobilization of CuO on the sand to yield a catalyst with excellent performance for treating organic pollutants in pregnant waters to meet technology-based treatment standards. The catalytic activity of the developed supported and unsupported catalysts is investigated with complete decolorization and/or degradation of the simulant contaminant (MO dye) within short periods (enhanced process kinetic), utilizing low hydrogen peroxide amounts, at ambient temperature, without UV irradiation, and enhanced catalyst durability are the main optimization parameters to achieve. Direct immobilization of the $CuAc_2.H_2O$ thermal decomposition products on the sand as support is the subject of this work. The effects of loading conditions, including decomposition temperature, cooling rate, quenching media, and $CuAc_2.H_2O$ to sand ratio, previous activation of sand, will be studied systematically. PXRD and its Rietveld refinement, SEM-extracted data, and statistical analysis of the obtained information are utilized to extract useful information to conclude the most prominent synthesis conditions. Evaluating and optimizing the catalytic activity for the degradation of organics-pregnant wastewater effluents, especially from dyes and textiles industries, are investigated, and the parameters' effects have been explored to optimize the reaction conditions. This work aimed to develop and adapt a simple, rapid, easy-to-implement, low-cost, efficient, suitable for massive production and application, and readily applicable method for treating colored, organics-pregnant wastewater effluents, especially from dyes and textiles industries.

2 Experimental Procedures

2.1 Materials and Reagents

Copper acetate monohydrate ($Cu(Ac)_2$). H_2O, manufacturer, and grade) is used as the active ingredient precursor. Methyl Orange (MO, manufacturer, and grade) is used as a recalcitrant azo dye simulant. 3% Hydrogen peroxide H_2O_2 oxidant stimulation. HCl, A.R., 37%, Fluka, and NaOH pellets, ACS reagent, Sigma-Aldrich were used for pH adjustments. All reagents were used as received without further purification.

3 Preparation, Synthesis, and Coating Conditions

Sand, normally used for construction purposes in AdDawadimi city, Kingdom of Saudi Arabia (KSA), is used as support. Sand particles were sieved, and the portion of the particle size range 250–500 μm was separated and used for the subsequent processing steps. The sand was washed and cleaned as follows:

a. Repeat wash and rinse with tap water three to four times.
b. Soak in acetone for 20–30 min and then decant the supernatant.
c. Wash with distilled Water.
d. Soak 20–30 min in diluted hydrochloric acid (HCl) and decant the supernatant.
e. Rinse with distilled water two times.

f. Dry sand at ambient temperature.

A predetermined amount of previously washed and cleaned sand, 20 g, was mixed well with 5 g $CuAc_2.H_2O$ in a dry clean porcelain pot, the ratio termed 5:20. The porcelain pot was then put into the furnace heated with 10 °C/min. up to the anticipated coating temperature, hold it there for one hour. Then, the furnace was turned off, and the coating mix was cooled according to an adopted cooling rate. The two adopted cooling schemes were slow cooling (SC) and air quench (Aq). The slow cooling was achieved by letting the sample cool inside the furnace after turning it off, following the cooling rate (≈ 2 °C/min., or more precisely, according to the equation: cooling time (minute) = $-0.8224T(°C) + 367.93$, $R^2 = 0.9247$). The fast cooling scheme, Aq, was achieved by quenching the sample into the air, which cooled rapidly with an approximate cooling rate of > 45 °C/minute (exact cooling rate follows the equation: Cooling time (minute) = $-0.0258T(°C) + 12.363$, $R^2 = 0.9722$), reaching the ambient temperature within approximately 10–12 min. According to these anticipations, many samples were synthesized as detailed with their corresponding preparation conditions in Table 1.

4 Follow-Up Methods

Discoloration extent was followed-up spectrophotometrically using a UV–Vis spectrophotometer (JENWAY 6850 UV/Vis. Spectrophotometer). In addition, changes in the parent molecule concentrations and the appearance of degradation products could be identified using the scan function from 190 to 600 nm. The hydrogen ion concentration (pH) changes were measured using a pH sensing electrode (Pasco-Scientific pH electrode) connected to a data logger (Explorer GLX, Pasco) via PASPort CHEMISTRY Sensor, Pasco-Scientific. The pH meter was operationally checked and calibrated whenever needed, following the manufacturer's guidelines. The temperature (T, °C) was measured using an independent electrode connected to the data logger via the Passport CHEMISTRY Sensor.

5 Characterization Techniques

The surface morphology of the prepared materials was probed using a scanning electron microscope (SEM) working at 5 kV (SEM, JOEL LA model). In addition, crystallographic characteristics and identification of the decomposition products were carried out using the powder X-ray diffraction (PXRD) technique on a D8 advanced Bruker XRD diffractometer operating with CuKα source of λ = 1.54056 Å at 40 kV and 100 mA in 2θ range 5°–80° with a step of 0.02°. The structural properties were explored, including samples' phase identification, crystallite size, hkl, matching phases quantification, and lattice parameters were assessed using Rietveld refinement with Profex 5.1.0 software. Surface porosity was estimated by surface area analyzer (Gemini VII 2390 Surface Area Analyzer—Micromeritics). The adsorptive gas was N_2, with an equilibration time of 10 s.

6 Results and Discussion

This work aimed to develop and optimize a simple, rapid, easy-to-implement, low-cost, efficient, suitable for massive production and application, and readily applicable method for treating colored, organics-pregnant wastewater effluents, especially from dyes and textiles industries. Each cascade step has its influencing factors, the associated response variables, and controlled optimization parameters (controlled variables). The relationship between them was studied systematically and thoroughly according to each experiment's specific anticipated output to include as many variables as possible. The parameters (controlled variables) affecting synthesis, loading, and subsequent simulant dye degradation reaction were investigated. Those controlled and the accompanying uncontrolled variables are depicted in Scheme 1. As seen in Scheme 1, the total number of variables is so great, which impairs the full factorial study of their effects. Hence, whenever deemed beneficial, statistical optimization techniques were implemented. A detailed description of each experimental set and the obtained results, comments, and discussions, are presented in their respective sections.

7 Structure, Composition, and Morphological Characteristics

7.1 Crystallography of the Catalyst-Coating

The powder x-ray diffraction (PXRD) spectra of the catalyst layer that was produced by direct staining quartz sand by the thermal decomposition products of $CuAc_2.H_2O$ are presented in Fig. 1. In addition, the PXRD spectra of pure decomposition products and quartz sand annealed at different temperatures are also included for comparing the differences in Fig. 1.

The PXRD spectra of quartz sand showed no disappearance or appearance of peaks among quartz sand dried at room temperature (RTS) or that annealed at 600 °C cooled rapidly (S600Aq) or slowly (S600SC). This indicated an unremarkable change in the chemical composition of quartz sand with annealing temperature. No characteristic peaks of $CuAc_2.H_2O$ or $CuAc_2$ appear, indicating complete acetate decomposition at all tested decomposition temperatures.

Table 1 Summary of the prepared samples and their synthesis conditions

No	Code	Activation Temp. (°C)	cooling rate	$CuAc_2.H_2O$: sand ratio	Remarks
1	CN600SC	600	Slow cooling	Pure $CuAc_2.H_2O$	Heated up to loading temp
2	CN500SC	500	Slow cooling	Pure $CuAc_2.H_2O$	Heated up to loading temp. and then air quenched
3	S600Aq	600	Air quench	Bare sand	Heated up to loading temp
4	S600SC	600	Slow cooling	Bare sand	Heated up to loading temp. and then air quenched
5	RTS	Room temperature		Bare sand	Only washed and dried at room temperature without heating
1	5400AQ	400	Air quench	5:20	Heated up to loading temp
2	5500AQ	500	Air quench	5:20	Heated up to loading temp. and then air quenched
3	5500SC	500	Slow cooling	5:20	Heated up to loading temp
4	5600SC	600	Slow cooling	5:20	Heated up to loading temp. and then air quenched

Scheme 1 Schematic diagram depicting the process' black-box

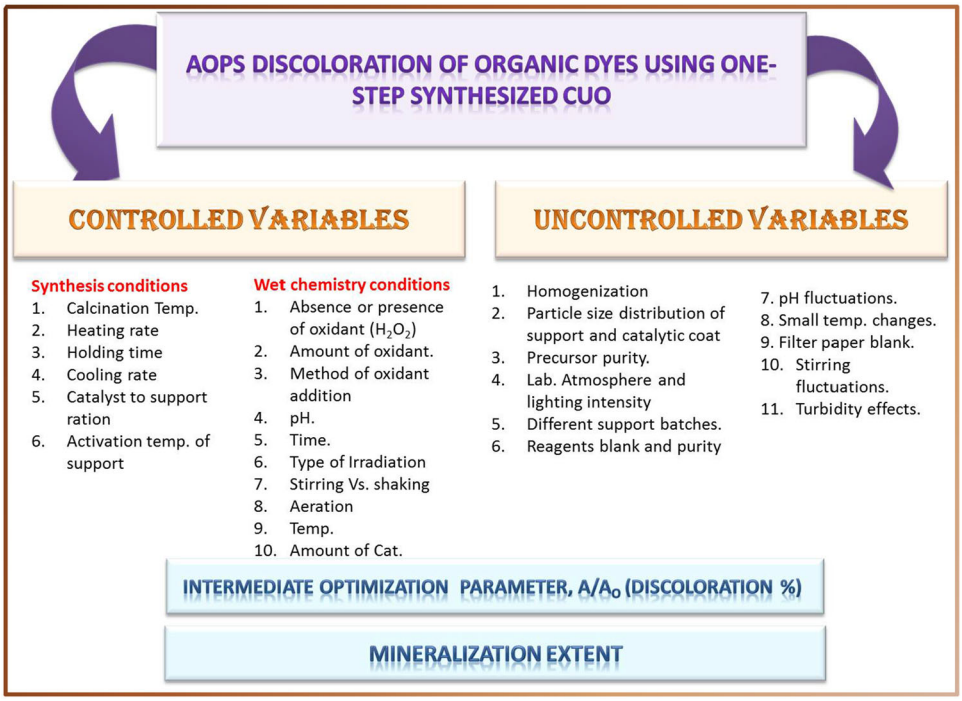

Based on a high-temperature XRD study, Bellini et al. [73] reported that $CuAc_2.H_2O$ lost hydration water at a lower temperature. Decomposition started at 200 °C and continued to 400 °C, leading probably to the co-formation of Cu_2O, and CuO amorphous phases, which crystallize to CuO in an oxidation process, agreeing with that reported by Lin et al. [74] of complete $CuAc_2$ decomposition at 310 °C [73, 74]. Distinct peaks with appreciable intensities are identified for cuprite (Cu_2O) with *hkl* indices 110c, − 200c, 200c, and 220c, Tenorite (CuO) with *hkl* indices 110t, 002t, 111t, 11–2t, 20–2t, 020t, 202t, 11–3t, and zerovalent metallic copper (Cu°) with hkl indices 111Cu, and 200Cu. Formation of the lower oxidation states products, Cu_2O and Cu°, may be reasoned to the imposition of in situ reducing environment as the acetate anion breaks down upon heating to produce CO and H_2 reducing gases [75, 76]. Lin et al., 2012; Naktiyok and Özer, 2019 studies show that employing TG/DTG and DTA, $CuAc_2$ finishes decomposition at about 310 °C with the formation of Cu°, Cu_2O, and CuO. They reported that the contents of Cu° and Cu_2O decrease gradually with increasing CuO from 310 to 510 °C [74, 77]. So, 400 °C was selected

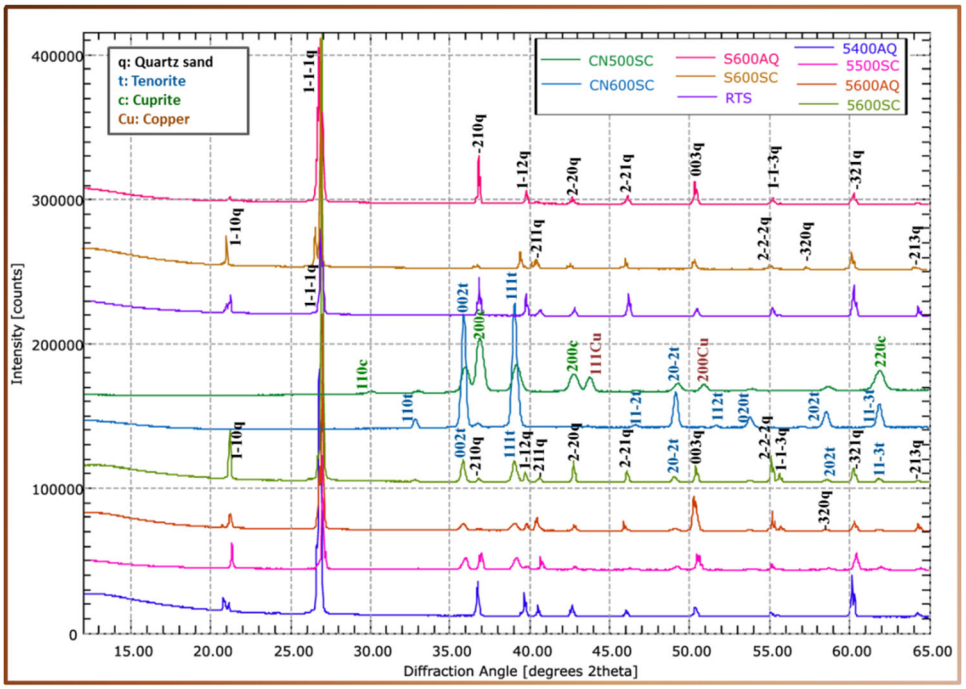

Fig. 1 Powder X-ray diffraction spectra of the catalyst-coating onto quartz sand and pure thermal decomposition products of copper acetate monohydrate. Conditions: test temperature: variable, hold time: 1 h, heating rate: 10 °C/min., cooling rate: variable

as the lowest coating temperature employed in this study to ensure complete decomposition and formation of crystal phases. However, the spectra for samples decomposed at 500 °C (CN500SC) still show the three phases with remarkable intensities, while that at 600 °C (CN600SC) involved no characteristic peaks for Cu° with very weak ones for Cu_2O, confirming the preferable formation of CuO at higher temperatures.

Interestingly, no characteristic peaks of Cu° or Cu_2O are seen in the catalyst-coating spectra, 5400Aq, 5500SC, 5600Aq, and 5600SC, at all temperatures and cooling rates experimented. This behavior may be explained as, when decomposing pure $CuAc_2.H_2O$, a sticky layer may be formed from the fine decomposition products as the produced gases have no sufficient pressure to effect the complete layer rupture, allowing the formation of in situ reducing pockets that lead finally to the formation of lower oxidation state products. But, in the presence of coarse quartz sand, the formation of such sticky crust at the top of the coating mixture could not be attained, allowing ease out-diffusion of reducing gases, CO and H_2, and the in-diffusion of air. In such a way, the establishment of in situ reducing pockets may be diminished, leading to complete oxidation to the highest oxidation state, CuO, as portrayed in Scheme 2. The presence and absence of this sticky crust were assured visually.

7.2 Rietveld Refinement of the Fabricated Catalyst-Coating

Visual inspection of the data set revealed that the spectra consist of sharp, well-separated peaks without too much overlap with a good signal-to-noise ratio validating the data set usability. The Rietveld refinement, developed more than 50 years ago, is an elegant method to resolve the problem of peak overlap. It is based on modeling a calculated powder diffraction pattern described by a set of parameters [78], enabling quantifying the phases' composition with the relevant structural parameters. In such a way, the variation of the lattice parameters, crystallite size, and unit cell volume with the experimental conditions can be probed and traced. In this study, Profex 5.1.0 software was utilized to accomplish the Rietveld refinement task by deconvoluting the overlapped peaks and quantifying the phases' relative proportions at different conditions. The prerequisite of any Rietveld refinement is identifying and matching the present phases by employing the search-match tool in Profex 5.1.0 and the help of QualX version 2.24. The monoclinic tenorite phase (Cu_4O_4) with a space group No. #15 and HermannMauguin = C2/c is the mainly identified catalyst-coating phase. The sand substrate was identified with the greatest peaks' intensity as quartz with spacegroupNo#152 and HermannMauguin = P3_121. No sample showed to contain cubic cuprite (Cu_4O_2) or cubic copper (Cu°), as seen in the case of thermal decomposition of $CuAc_2.H_2O$ in the absence of sand support, as mentioned above.

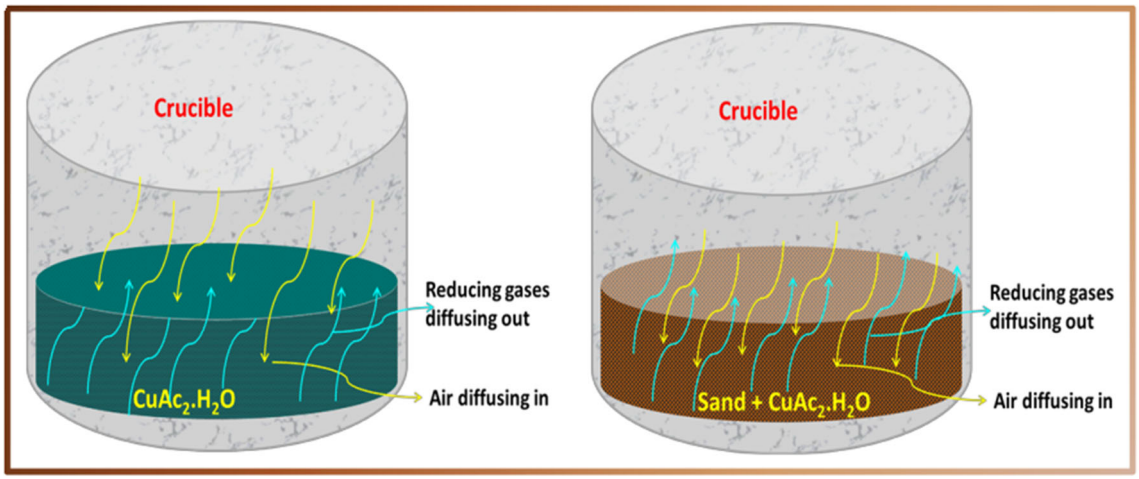

Scheme 2 Schematic depiction Portraying the gaseous product flows

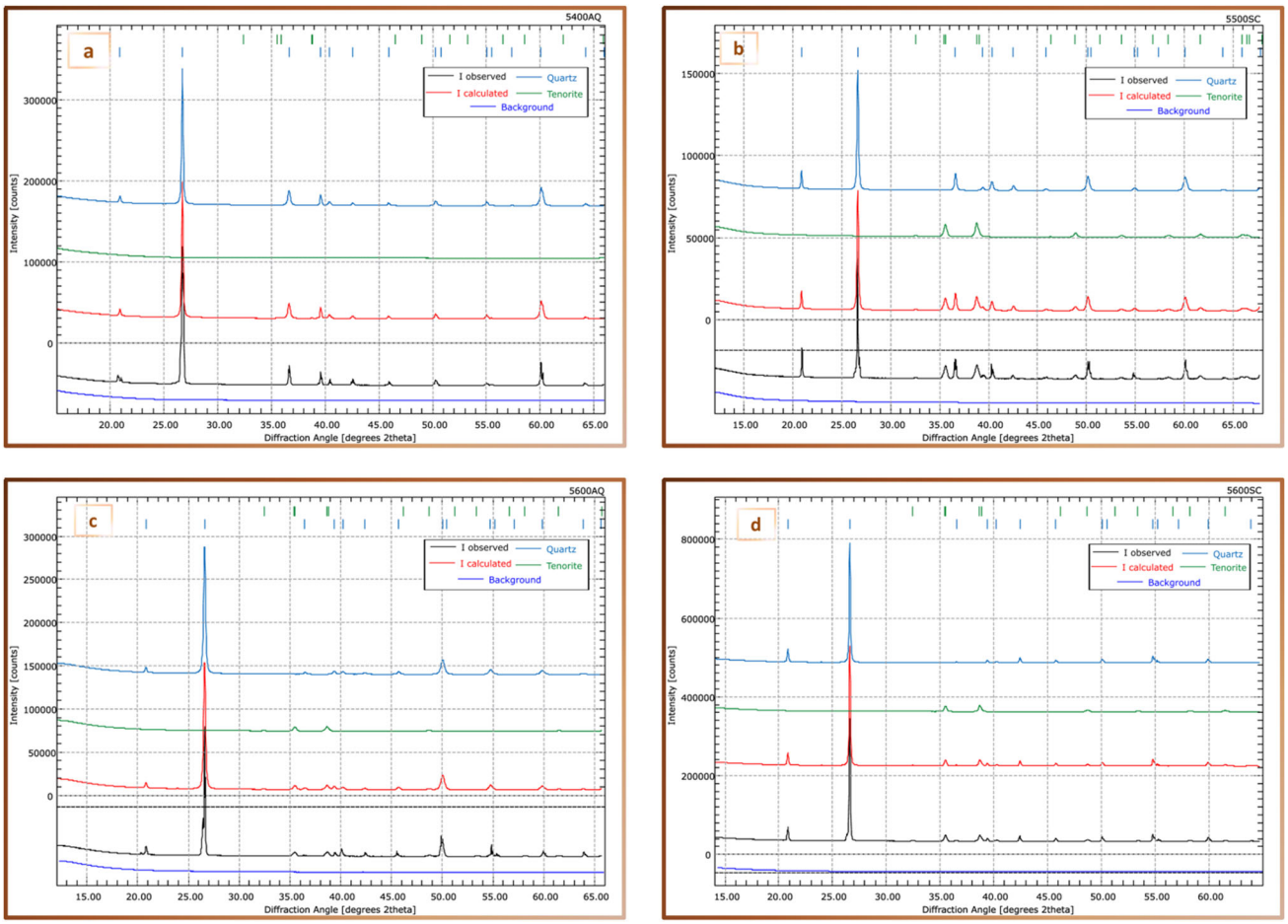

Fig. 2 Deconvoluted Powder X-ray diffraction patterns of the catalyst-coating onto quartz sand. "Conditions: test temperature: variable, hold time: 1 h, heating rate: 10 °C/min., cooling rate: variable

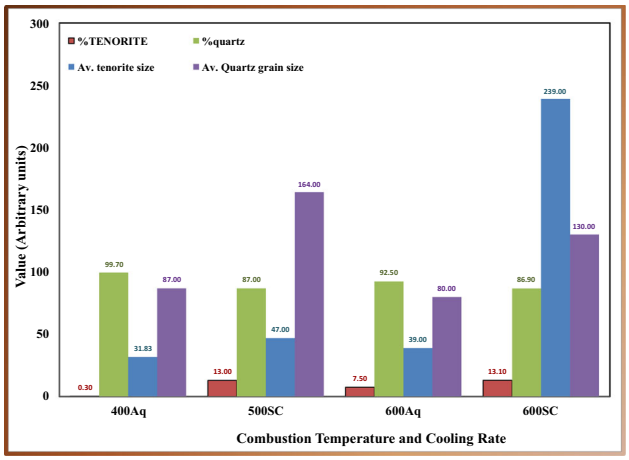

Fig. 3 Graphical summary of Rietveld refinement extracted crystallography

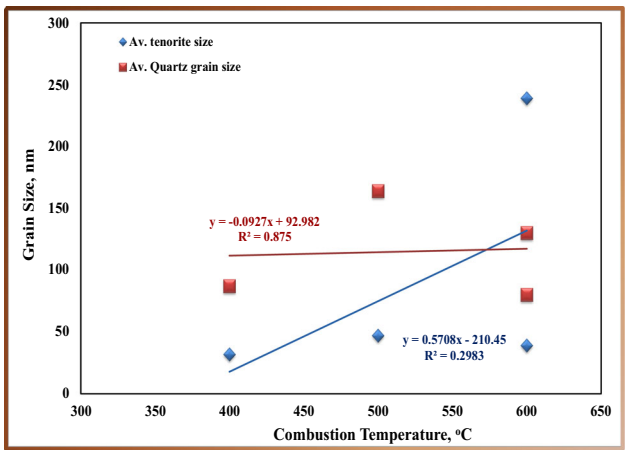

Fig. 4 Changing of grain sizes with combustion temperature and cooling rate

The deconvoluted Powder X-ray diffraction patterns of the catalyst-coating onto quartz sand are shown in Fig. 2. The spectra have no characteristic peak of $CuAc_2.H_2O$, assuring the complete decomposition of $CuAc_2$. The influence of the cooling rate and the decomposition temperature on the crystallinity of the catalyst-coating was studied. Thermal decomposition temperatures examined were 400, 500, and 600 °C, with two cooling schemes of slow cooling (SC) and air quench (Aq), and holding time at maximum temperature was set for one hour with a heating rate at 10 °C/minute for all experiments. Figure 2 shows the Rietveld refinement's deconvoluted spectra. The current work's ultimate goal is to optimize the coating conditions rather than the complete evaluation of the crystallography of the products. The deconvoluted peaks explore remarkable changes with the AT increase, as no observable peaks are seen at 400 °C and Aq, Fig. 2a, of the catalyst-coating. This theme may be due to thinner layer formation with a lower crystalline share supported by the amorphous phase in the SEM images. The samples calcined at higher temperatures showed distinct characteristic peaks of the catalyst-coating, namely Tenorite, with no peaks for Cu° and cuprite, confirming complete oxidation of the decomposition products to CuO at all temperatures higher than 400 °C. Tenorite phase, as the active ingredient, ramped from 0.3% at 400 °C and Aq to 13% at 500 °C and Aq. However, at 600 °C and Aq, the Tenorite percentage decreased to 7.5%, then ramped up to 13.1% at 600 °C and SC. Although these percentages may not reflect the actual share of the catalyst-coating to quartz, it represents a good ground for comparison purposes. The mixture was initially prepared ($CuAc_2.H_2O$/sand is 5:20) to yield about 9% of CuO to quartz. A graphical summary comparing the percentages of the Tenorite phase and grain size is given in Fig. 3. The grain size of Tenorite showed a mild increasing trend with temperature and a more rigid ramping with changing cooling scheme from Aq to SC, Fig. 4. As evident from Fig. 4, the Tenorite average grain size exhibited mild dependence on calcination temperature and far exacerbation with slow cooling for the sample calcined at 600 °C. The descriptive statistics of the different crystal phase parameters are summarized in Table 2.

8 Statistical Analysis of the Data Obtained from Rietveld Refinement

Descriptive statistics of the phases percentages and the grain sizes are summarized in Table 2 and Fig. 5. Tenorite's average grain size did not follow the normal distribution (p-value < 0.05 according to the Anderson–Darling test) with positive Skewness as it tends toward the heavier tail (i.e., larger grain sizes). Moreover, the positive Kurtosis values demarcate that the distribution has a sharper peak than the normal distribution, possibly due to the low number of samples represented statistically. However, the sharp growth of the Tenorite grain size at the boundary conditions tested, i.e., 600 °C. Such a theme may point out that there is a systematic growth of the grain sizes with the calcination temperature rising, leading to that deviation from the normal distribution pattern. This may infer the dependence of tenorite grain sizes on AT in direct proportion and CR since it grows rapidly with the cooling rate slowing. The median is far lower than the Q3-values and the maximum value, indicating an extreme value in the heavier fringe (i.e., 239 nm at 600 °C and SC). This may lead to concluding the preference for fast cooling and the lowest calcination temperatures for yielding smaller Tenorite grain sizes.

On the contrary, quartz grain size followed the normal distribution with Skewness values approaching that of typical

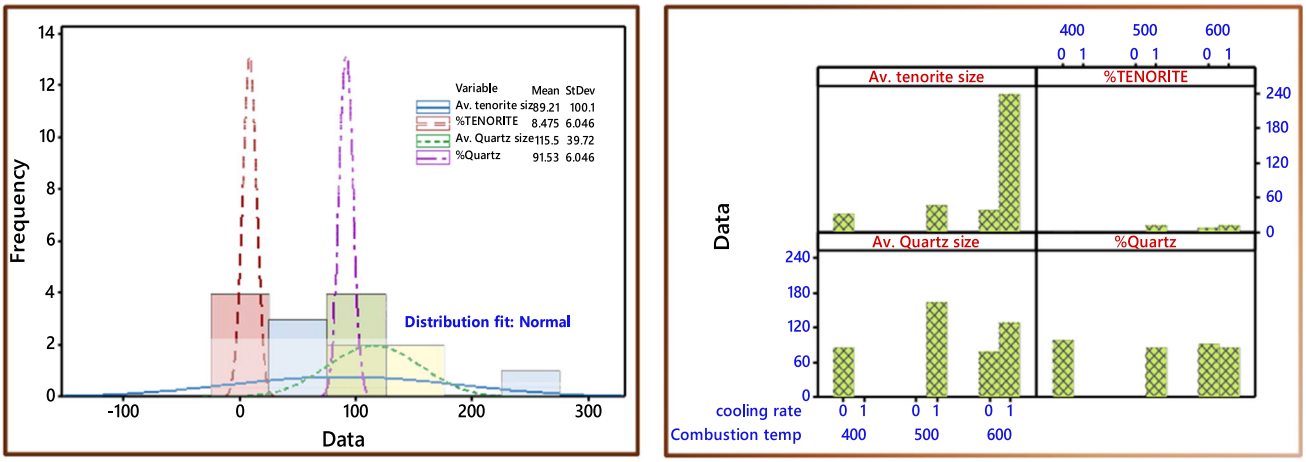

Fig. 5 Tenorite and quartz quantities and grain sizes distribution extracted from Rietveld refinement

Table 2 Descriptive statistics of the samples' characteristics extracted from Rietveld refinement

Variable	Mean	SE Mean	SD	Min	Q1	Median	Q3	Max	Range	Skewness	Kurtosis	And. Darl[a] *P*-value
Av. Tenorite grain size, nm	89.20	50.00	100.1	31.8	33.60	43.00	191.00	239.00	207.20	1.98	3.92	0.71 0.017
%TENORITE	8.47	3.02	6.05	0.3	2.10	10.25	13.07	13.10	12.80	− 1.07	− 0.16	0.36 0.242
Av. Quartz grain size, nm	115.50	19.90	39.7	80	81.80	108.50	156.30	165.00	85.00	0.60	− 2.39	0.28 0.42
%quartz	91.53	3.02	6.05	86.9	86.93	89.75	97.90	99.70	12.80	1.07	− 0.16	0.36 0.242

[a]Anderson-Darling A-squared value

normal distribution. The mean and median values are comparable for % quartz and average quartz grain size, indicating that the data set is extremes-free. However, the Q3 and the maximum values are comparable, demarcating the data set shift to the heavy right tail. Mild standard deviation values, ≈ 40 nm, compared to 100 nm for Tenorite grain size, refer again to an extremes-free data set for quartz. The negative Kurtosis value for quartz grain size demonstrates flattening than the normal distribution due to the occurrence of the maxima at the data set middle, not at the boundary line as in the case of Tenorite grain size. However, the trend of grain size growth with slow cooling is obvious.

The matrix plot, Fig. 6, demonstrates the interactions among the experimental variables with the average Tenorite grain size as the response parameter. Figure 6a shows the interaction matrix plot among the dependent variables to demonstrate the pattern of their interdependency. As shown, the average Tenorite grain size is directly proportionate to % Tenorite with a sudden steep propagation at the sample 5600 SC, resulting in the largest % Tenorite, 13.1%. However, sample 5500SC has approximately the same% Tenorite, 13%, giving an average Tenorite size much smaller, 47 nm, compared to 239 nm for 5600 °C, indicating that the Tenorite percentage may not be responsible and another factor is the significant influence, probably the calcination temperature. The other dependent factors show no specific relationship except that there is generally a clear trend of growing grain sizes, Tenorite, and quartz, slowing the cooling process as the grains have a larger time to grow than in the air-quenching cooling scheme. Figure 6b explores the interaction plot with the response parameter, average Tenorite grain size, with the smaller being the best. Calcination temperature and cooling rate significantly influence the response parameter, but unfortunately, contradictory trends in terms of average tenorite grain size and % Tenorite. The Aq cooling path yields Tenorite with smaller grain size, while SC gives rise to larger sizes, especially when the AT exceeds 500 °C, i.e., 600 °C. AT Average Tenorite grain size proportionate directly to % Tenorite, with the CR showing an excursion from Aq to SC at 600 °C. As the highest Tenorite percentage

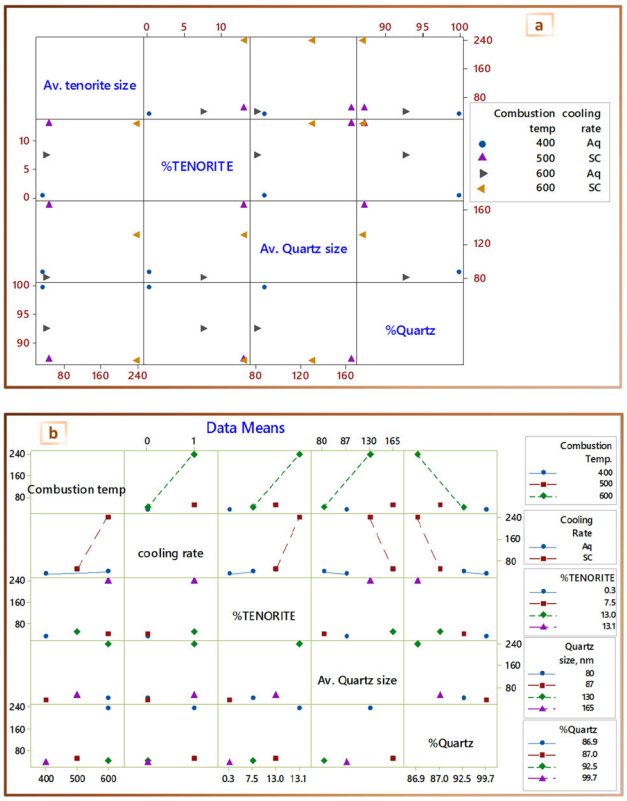

Fig. 6 Interactions plots. **a** Interaction matrix plots of the dependent variables; **b** Interaction plot for average Tenorite grain size, nm, as the response

and smaller grain sizes are preferred, the interaction matrix suggests that the samples have to be processed at lower temperatures than 600 °C and the SC cooling scheme. A more tuned positioning of the optimum conditions is presented hereinafter. The plots are informative, leading to deduce that the system is sensitive and prone to the experimental variables within the tested ranges. The effects of the variables are not unidirectional, necessitating some trade-offs to probe the optimum conditions, with the AT and CR being the only controllable variables while others are interdependent.

The main effects plots for the average Tenorite grain size and % Tenorite are presented in Fig. 7. The plots emphasize the abovementioned findings as Tenorite grain size prp[gated exceptionally at 600 °C with a great reduction in % Tenorite at Aq cooling, recommending employing lower calcination temperature and an intermediate cooling scheme in between Aq and SC. Although Aq gave rise to smaller Tenorite grain sizes at all CTs, the coating layer is expected to be stressed as insufficient time is available for tempering, which may affect the layer leachability and hence, the catalyst recyclability. So, a trading-off is required again.

Figure 8 portrays 3D surface plots of the controlled variables" effects on the average Tenorite grain size, Fig. 8a, b, and the %Tenorite (Fig. 8c). As evident, AT and CR affect the Tenorite grain size with a sudden and sharp increase at 600 °C and SC. Unfortunately, % Tenorite showed a reverse trend with a larger share in the case of SC, whatever the AT was. To explore the existence of reasonable trade-offs, the dynamic response optimizer tool is recruited. Figure 9 shows the conditions directing the responses out of the non-desirability range, yielding reasonable compromise among the interplaying factors. The optimum immobilization conditions may be AT: ≈ 485 °C; CR: SC. It is worth noting that the ultimate optimum operating conditions are a function of many variables, which have to be updated accordingly with moving on to evaluating the properties of the fabricated material. After this, the morphological properties of the immobilized catalyst are investigated.

9 Morphological Features

The morphological characteristics of the immobilized catalyst onto sand were investigated employing the SEM technique. Figures 10, 11, 12 present the SEM micrographs, the 3D visualized view produced employing the Gwyddion 2.62, the ImageJ 1.53t software interpolated surface plot, and the graphical summary of the descriptive statistics concerning particle size distribution extracted from the SEM micrographs using ImageJ 1.53t software. The surface plot was generated employing the ImageJ v1.53t utilizing the interactive 3D surface plot V3.0.1 plugin, which interprets the luminance of each pixel in the image as a height for the plot [79]. This way, different views can be obtained with different magnifications, providing a reasonably readable visual inspection of the sample's surface irregularities. As confirmed by PXRD spectra, the sample calcined at 400 °C was not included as it contained minor amounts of crystalline Tenorite. All samples exposed well-dispersed, spheroid-like shapes of crystalline particles and a multilayer of tight catalyst-coating covering the whole surface of the underlying sand support. Sample 5600SC showed an intense agglomeration tendency, with minor amounts appearing rod-like.

Figure 10b presents the 3D view created, which helps mark the particles' surface roughness, distribution, and compactness. Mean roughness (S_a) was calculated as the differences between the sum of absolute data values from the mean height irregularities. The sample 5500SC surface roughness was estimated as 0.0726 with a Skewness of 0.112 and − 0.398 excess Kurtosis. The Skewness and excess Kurtosis values denote that roughness is normally distributed; hence, the particle's surface morphology is evenly distributed. Moreover, this roughness value is comparable to that of the bare decomposition products of $CuAc_2.H_2O$, evaluated as 0.0613. Overall, those findings confirm the complete surface coverage of the sand substrate with no remarkable holes or caves in

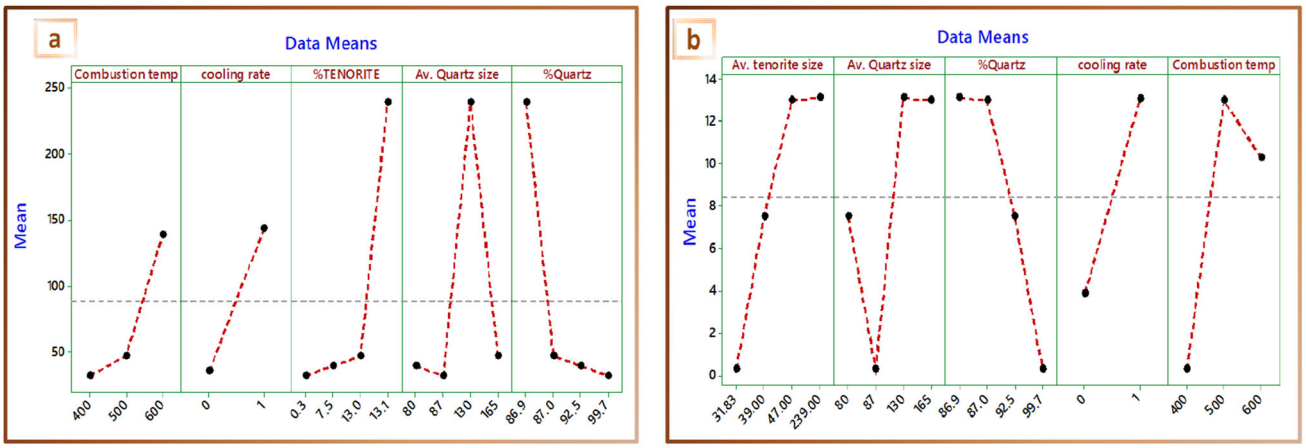

Fig. 7 Main effects plot for average Tenorite size and % tenorite as the response variables. **a** Average Tenorite grain size, nm; **b** % Tenorite

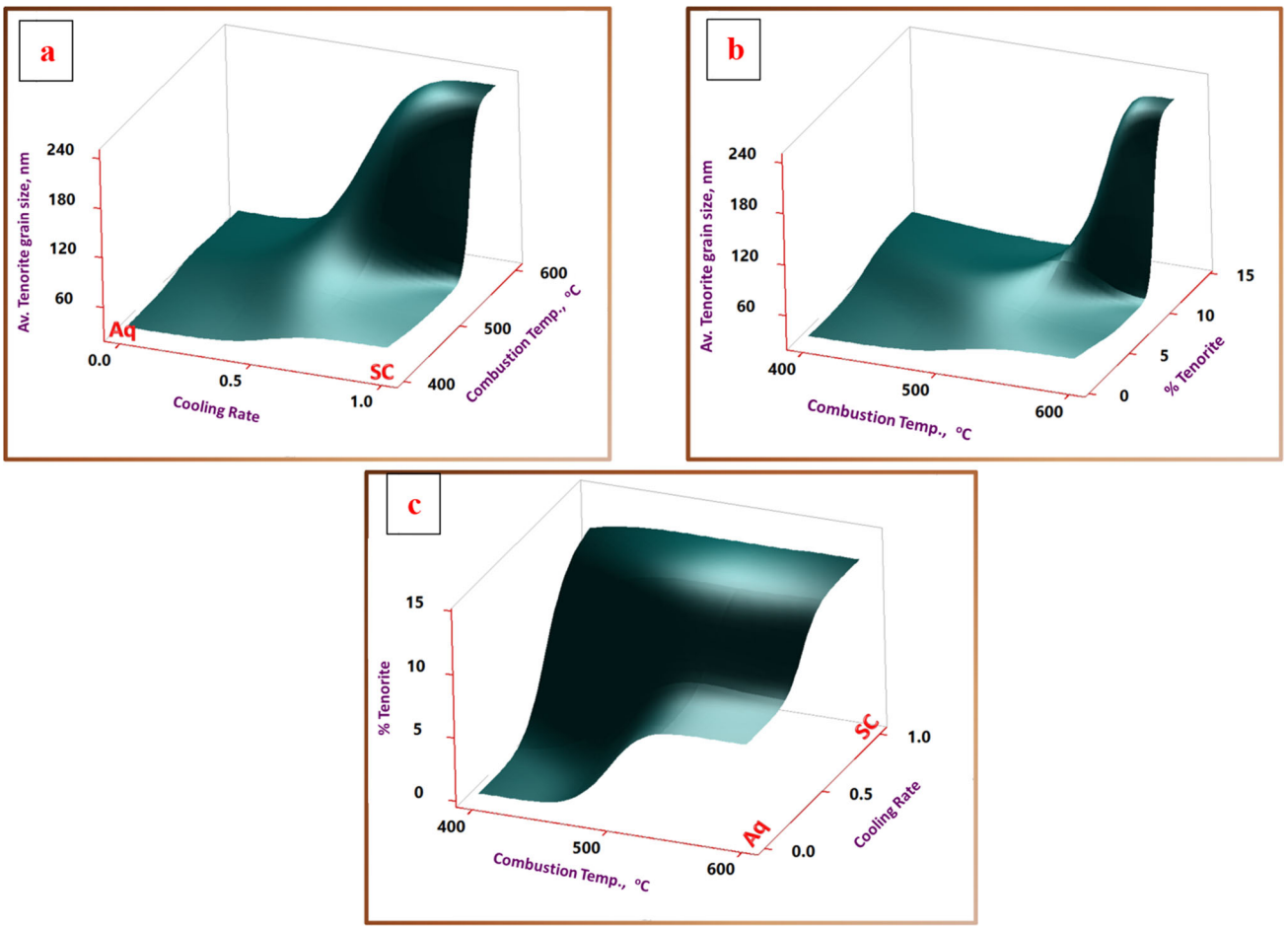

Fig. 8 3D surface plots of the interplaying factors on the average Tenorite grain size and % Tenorite

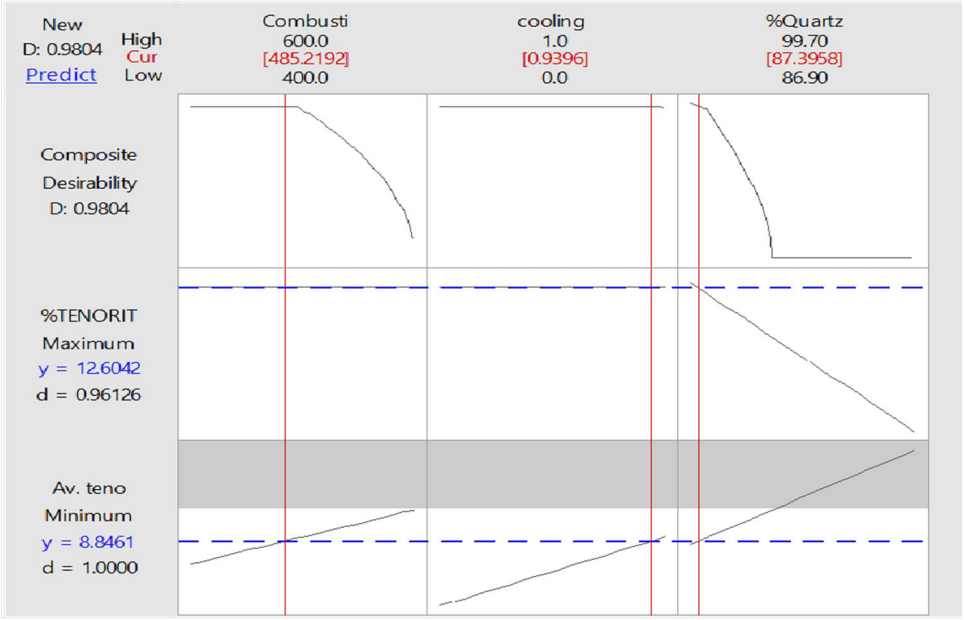

Fig. 9 Dynamic response optimizer of the influencing factors to yield the anticipated outputs

the coating. The surface plot, Fig. 10c, generated by the 3D surface plot V3.0.1 plugin of the ImageJ v1.53t. The plugin interprets each pixel's luminance as a height in the image and generates the interactive plot [79]. Hence, different views can be reasonably obtained at different magnifications, allowing readily interpretable sample surface irregularities from direct visual inspection. Figure 10c demonstrates that bare areas of the support are limited, red-colored regions. Most of the surface is green-colored, marking densely coated, i.e., multi-layered, regions. The yellow-colored portions denote the thin coating, while the blue-colored ones are limited but evenly covering the whole shoot of X30,000, indicating the particles' edges intersection, i.e., agglomerated clusters. Limited far-distanced red-colored spots evidence compactness and surface coverage. The higher resolution shoot, with 30 K magnification, clarified in more detail the pixels' distribution pattern, the clustering tendency, and associated surface roughness. The catalytic surface coating exposed very limited porosity.

A graphical summary of the particle size distribution statistics, Fig. 10d, shows that the mean particle size is 528 ± 248 nm. The normality distribution test, Anderson–Darling, has a p-value < 0.005 for a 95% confidence level test indicating the rejection of the null hypothesis concerning the normal distribution of the data histogram of particle size distribution exhibits a remarkable difference between the median (643.85 nm) and mean (565.23 nm), indicating a drift toward the larger particle sizes emphasized with a high standard deviation (SD) values of ± 248 nm. The range value, 803.41 nm, indicated a widening distribution with the median and the 3rd quartile closer to the maximum, confirming the enlargement tendency of the grain with slow cooling. The less number of smaller size particles may be attributed to arise from the grains that are caged at the intersections or in a cluster hindering the grain growth. Although the data are non-symmetrical, the Skewness statistic is low (− 0.48) as the data approach mirrors each other at the two fringes. Such a trend may be explained as the particle size was not determined by the cooling rate alone, and the final growth depends on the initial size and the temperature gradient, clustering, and the space available for grain to grow. Moreover, it seems the support has a role in such distribution as at the same conditions without sand support, the particle size distribution did not show the mirrored shape and skewed toward the higher fringe with a much larger particle size (data not shown). The distribution has lighter tails than the normal distribution as it showed a negative Kurtosis value (− 1.32) which may be viewed as the temperature goes down below a certain limit, the particle growth is slowed or even diminishing since if it continues, there might be a wider size distribution (lower Kurtosis) than that observed.

Figures 11a and 12a exhibit almost the same trend and distribution as the previous sample. All the 5600Aq sample SEM showed the highest surface coverage to the sand support with apparent lower agglomeration tendency with well-dispersed spheres, while 5600SC exhibited mild agglomeration tendency with rod-like minors and bare spots of the sand support. The 3D visualized views in Figs. 11b and 12b show that the sample 5600SC exhibits higher surface roughness (0.1259) compared to (0.062) for the sample 5600Aq. This difference in Sa may be due to the bare spots in the case of 5600SC, as those bare spots give a higher difference for the pixels. The surface plots in Figs. 11c and 12c confirm the observations of complete surface coverage but hint at longer hairs

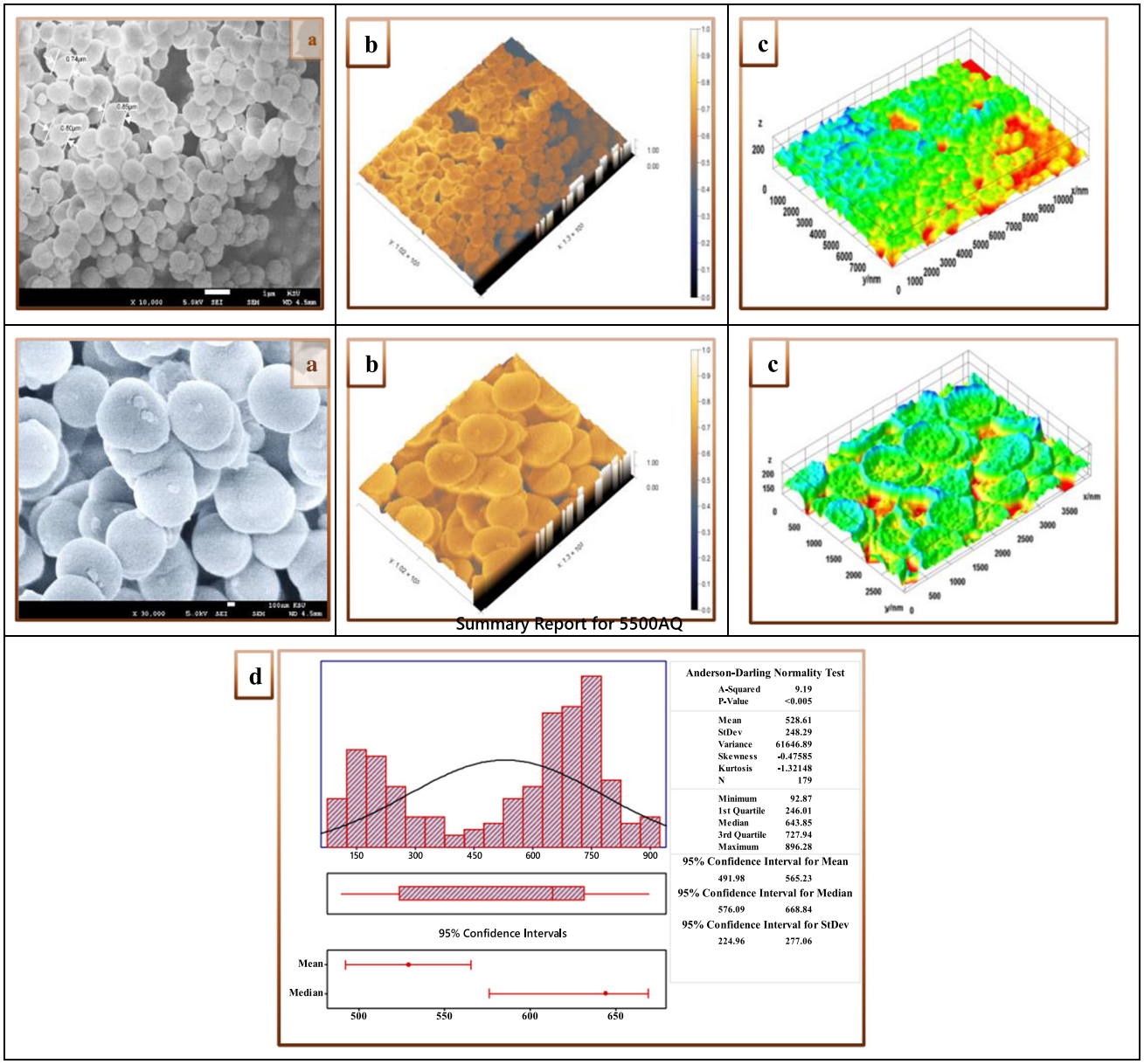

Fig. 10 SEM micrograph, 3D visualized view, surface plot, and the descriptive statistics graphical summary of the sample combusted at 5500SC. SEM micrographs of the samples calcined at 600 °C, (5600Aq and 5600SC) are shown in

for the particles (i.e., higher roughness) for 5600Aq than 5600SC corroborating the postulation that higher Sa computed may be in error due to the bare spots in case of 5600SC sample. Graphical summaries and the descriptive statistics of the distribution shown in Figs. 11d and 12d are similar to those of sample 5500SC, Fig. 10d. Particle sizes in all samples are non-normally distributed, non-symmetrical with mirroring at both sides and hence, their Skewnesses and Kurtosises values are comparable with tails shorter than expected for normal distribution. However, the mean, median, range, and quartile statistics follow an ascending order with increasing AT and decreasing CR. The means and SDs are 435 nm ± 232 nm and 631 nm ± 225 nm for 5600Aq, and 5600SC, respectively, and the medians are 589 nm and 750 nm, respectively. The Anderson–Darling A-square statistic and Kurtosis are inversely changing with the calcination temperature, indicating approaching normal distribution with increasing temperature, i.e., the crystal system approach maturity. Such particle size trends and values are comparable to Pookmanee's et al. 2019 findings calcined the precursor by microwave at 600–800 Watt for 6 min [80] and Dörner et al. [50] treated with ammonium carbonate and

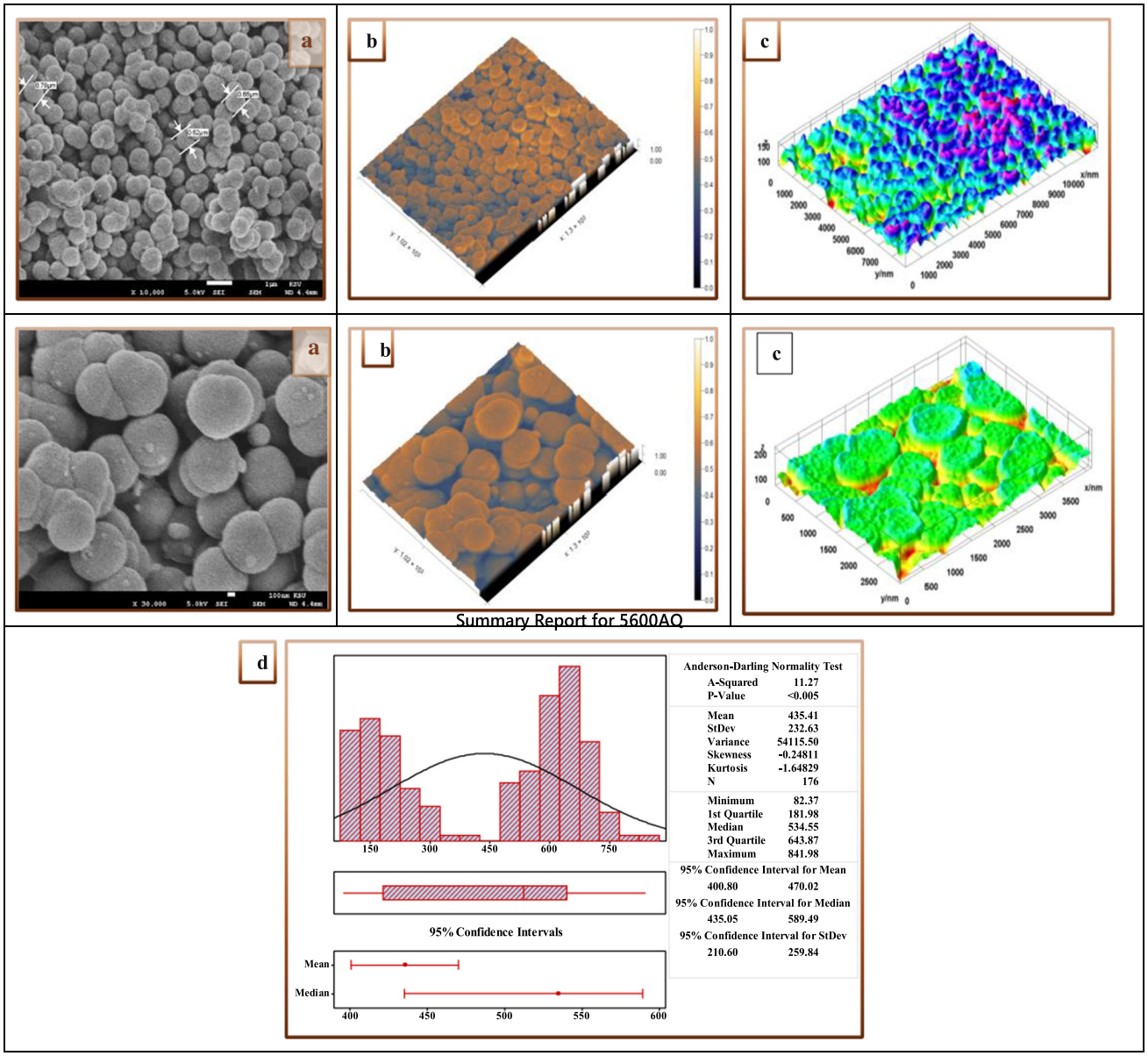

Fig. 11 SEM micrograph, 3D visualized view, surface plot, and the descriptive statistics graphical summary of the sample combusted at 5600Aq

calcined at lower temperatures (400 °C). Figure 13 summarizes graphically the statistics of the data extracted from SEM micrographs processing.

10 Textural Features

SEM micrographs show that the fabricated material is very poor in terms of porosity. This chapter presents the results of investigating the porosity and pore structure employing N_2 sorption measurements at 77 K. The isotherms that characterize the physical adsorption of gases by non-porous solids are the exhibited ones approaching the Type-II Adsorption with very limited quantities of the adsorbed ga. The samples' adsorption profiles demonstrate no hysteresis loops that may conclude that they are non-porous. Moreover, the amounts of adsorbed gases are very limited, marking weak physical attraction forces to the adsorbed gas and limited surface area. The BET surface area (S_{BET}), Langmuir surface area (S_{Lang}), adsorption average pore width, *t*-Plot micropore volume, and other obtained parameters are summarized in Table 3. The largest S_{Lang} reported is that of the 5500SC sample, and it decreased with increasing temperature and decreasing the cooling rate. The fabricated catalyst yielded limited S_{lang} of 2.82, 2.24, and 1.69 m^2/g for 5500SC, 5600Aq, and 5600SC samples, respectively. These limited surface areas

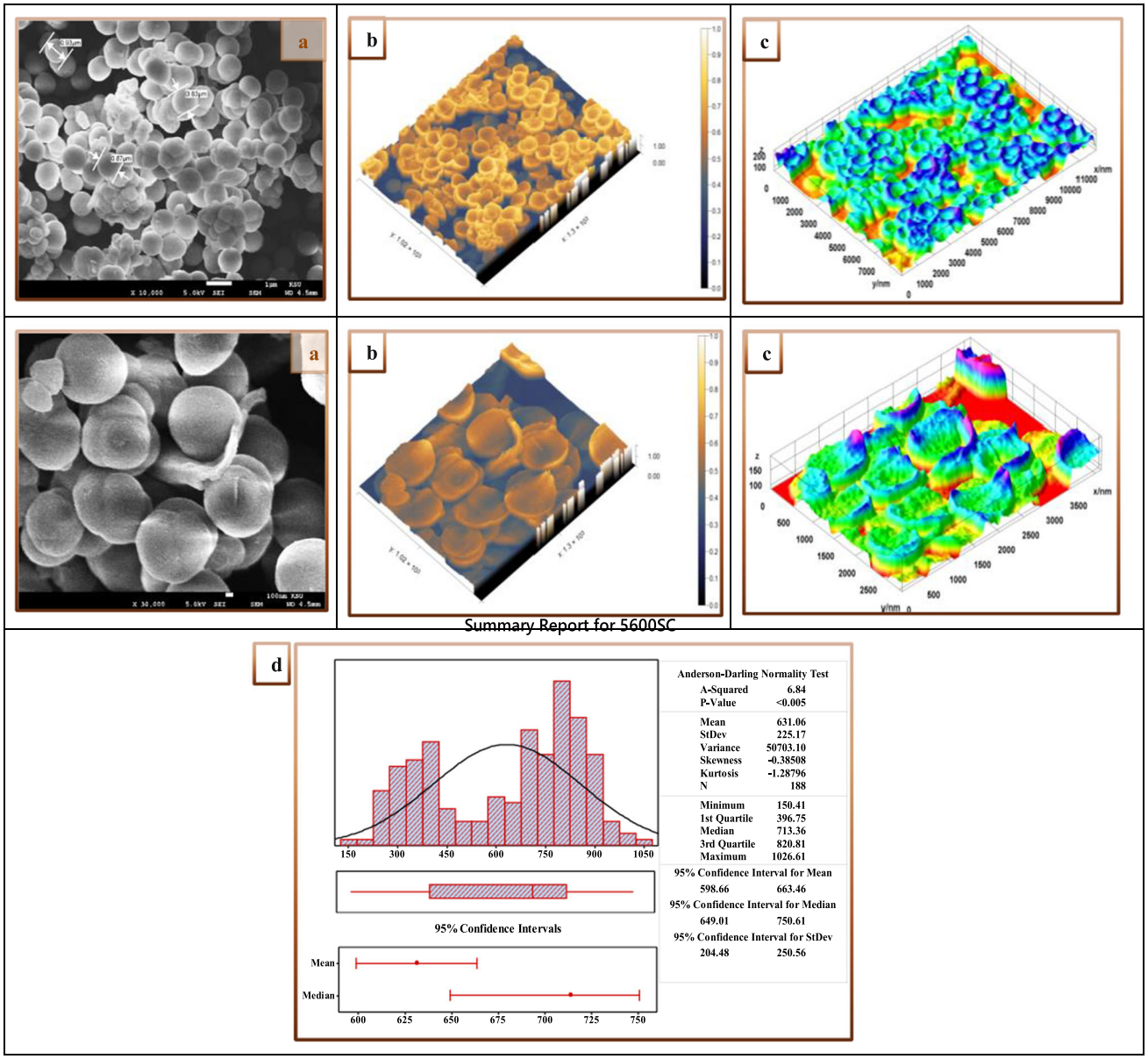

Fig. 12 SEM micrograph, 3D visualized view, surface plot, and the descriptive statistics graphical summary of the sample combusted at 5600SC

may be attributed to the high-sphericity of obtained coatings (the sphere has the lowest surface area to volume ratio), formation of aggregates and multilayers of the coating, larger particle sizes, and very shallow pores or even non-porosity. However, the sample 5500SC gave the largest S_{Lang}, while the 5600Aq sample had the smallest particle size and lowest agglomeration tendency. These findings suggest optimizing the synthesis conditions to lower the particles' agglomeration and size. However, the catalytic behavior must initially be evaluated to fabricate a fit-for-purpose material. The next section presents the axiomatic design of the experimental setup and the results of decolorizing the azo-dye solutions that are simulant for organics-pregnant wastewater effluents, especially from the dyes and textiles industries.

11 Screening and Optimizing the Control Parameters

Herein, the preliminary results that demonstrate the promising performance of the fabricated material toward the degradation of methyl orange azo-dye are presented. The detailed wet-chemistry experiments, process kinetics, optimization, and mechanism of action will be presented in separate work

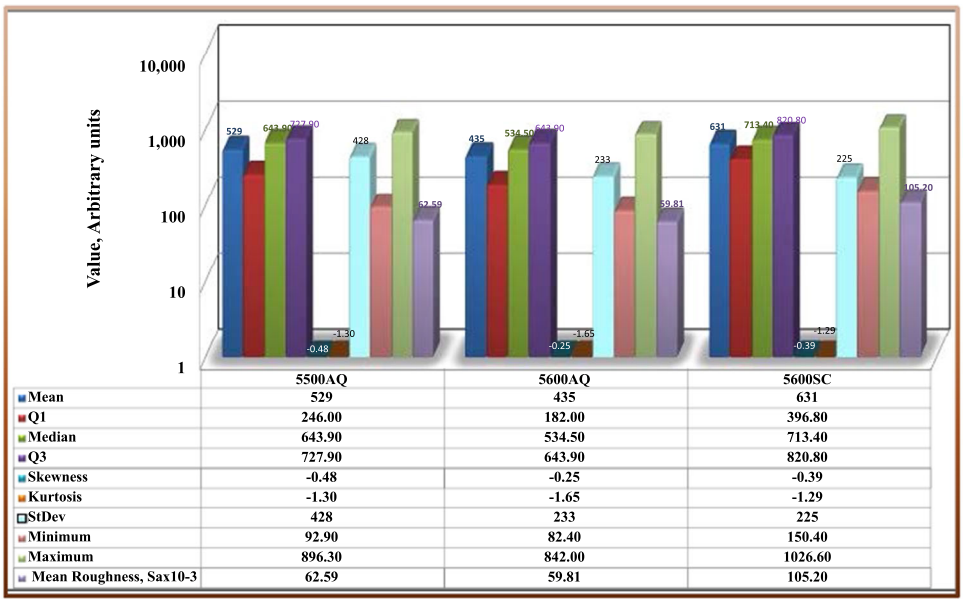

Fig. 13 Graphical summary comparing the descriptive statistics of SEM-extracted data

Table 3 Summary of data extracted from N_2 gas adsorption at 77 K

ID/Parameter	5500SC	5600Aq	5600SC
Single point surface area at $P/Po = 0.15$, m^2/g	0.4833	0.6188	0.6458
BET Surface Area, m^2/g	1.1334	1.1754	1.0281
Langmuir Surface Area, m^2/g	2.82	2.2391	1.6911
Single-point adsorption total pore volume of pores less than 19.876 Å diameter at $P/Po = 0.15$, cm^3/g	0.000202	0.000259	0.00027
t-Plot micropore volume, cm^3/g	− 0.000198	− 0.000231	− 0.00029
Adsorption average pore width (4 V/A by BET), Å	7.1361	8.8105	10.5131
Average particle size, Å	52,935.95	51,044	58,359.13
BET surface area report			
Qm, cm^3/g at STP	0.2604	0.27	0.2362
C	4.7367	6.7188	9.635
Slope, g/cm^3 at STP	3.0298	3.152	3.795

to avoid lengthy. The catalytic activity of the fabricated material (CuO-coated sand) was tested at different conditions to decolorize methyl orange (MO) solution of 19.46 mg/L MO (10 mg-C/L), using hydrogen peroxide as an oxidant. The pure CuO powder and CuO immobilized onto sand support are compared. A multilevel factorial design of an experimental set was devised and conducted to investigate the fabricated materials' relative performance in removing methyl orange (MO) azo dye. The experimental set was of mixed-level design where the control factors have different numbers of levels. The mixed-level factorial design has been chosen to estimate the significance of the main and interaction effects [81]. Another batch of experiments was carried out to investigate the kinetics of the MO removal process.

The multilevel factorial experimental set was conducted by fixing the untested variables at preselected arbitrary levels, including sample volume: 50 mL; concentration: 10 mg-C/L(≈ 20 mg MO/L); No irradiation; and continuous stirring at room temperature. The reaction time was arbitrarily fixed at 20 min. This strategy was followed to provide preliminary prove the fabricated material efficacy in degrading the organic contaminant simulant. A separate article will be devoted to thorough optimization, process kinetics, and reaction mechanism investigations. The analysis charts of the multilevel factorial experimental design response are given in Fig. 14. The difference between a catalyst and another is the annealing temperature, and the cooling rate at which the coating process was conducted is termed the catalyst type variable. The Pareto chart, Fig. 14a, shows that the catalyst type variable significantly influences the process response, with the second influencer being its interaction with pH. The amount of catalyst and hydrogen peroxide at the tested levels

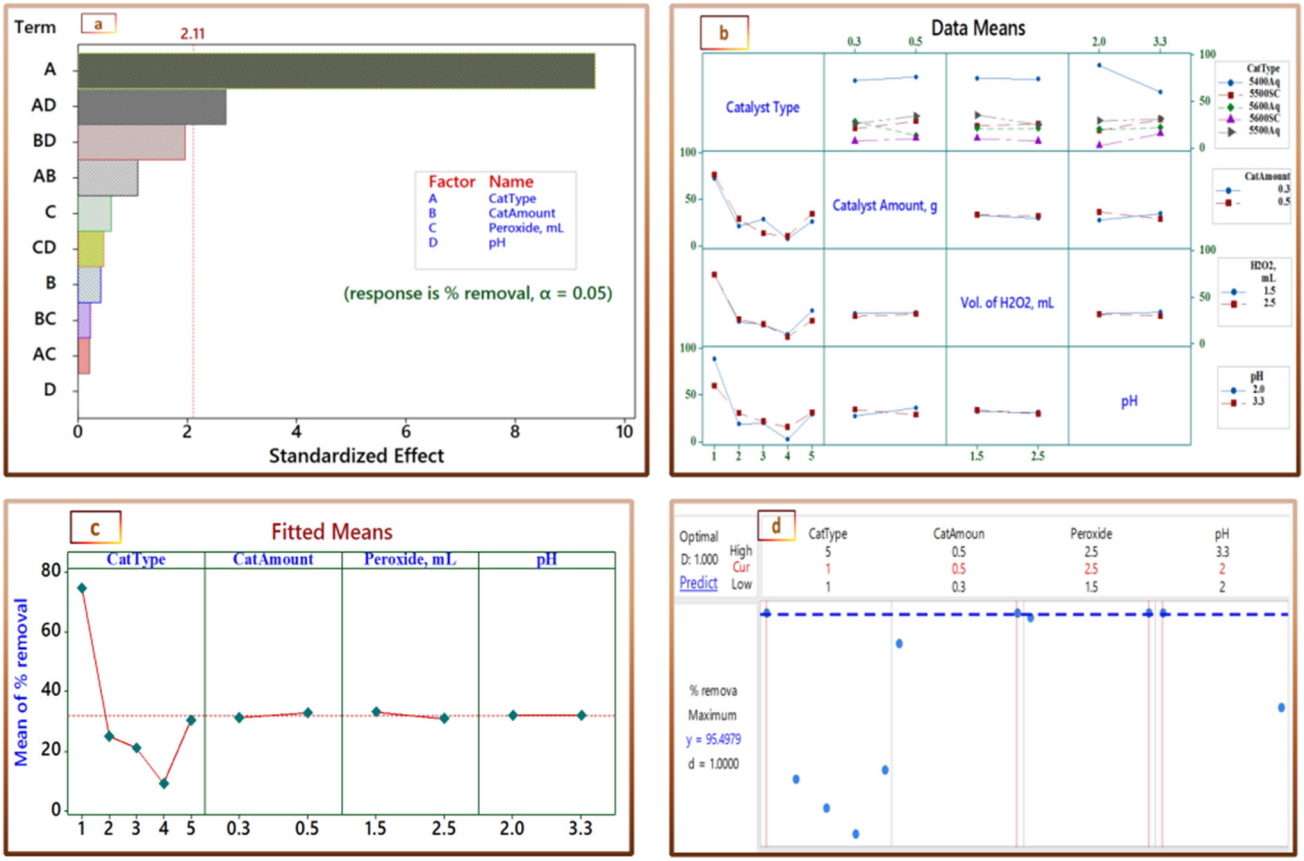

Fig. 14 The analysis charts of the multilevel factorial experimental design response. **a** Pareto plot; **b** main effects plot; **c** interactions plot, and **d** dynamic optimization plot. Conditions (variables fixed at pre-selected arbitrary levels): sample volume: 50 mL; concentration: 10 mg-C/L(≈ 20 mg MO/L); No irradiation; reaction time: 20 min; and continuous stirring at room temperature

showed little effect on the process response changes. However, the interaction terms explore a greater influence than being individual, implying the amenability of the process to the control variables that have to be studied and optimized collectively without omitting the ones that may seem insignificant erroneously. The interaction plot for % removal (decolorizing) as the response, Fig. 14b, delineates the dominance of the catalyst type control variable over the others providing much more information concerning the way of effective and demarcating which one performs the best and the worst. The sample 5400Aq, calcined at 400 °C (the lowest tested) and cooled by air quench, gave the highest % removal. Moreover, the interactions among each pair of the control variables explore the good performance of the lower pH and larger catalyst amount on % MO decolorizing. The amount of peroxide at the two levels tested showed no remarkable difference. The main effects plot shown in Fig. 14c emphasizes the predominance of the catalyst type factor and the milder influences of catalyst amount and peroxide amount. Figure 14d explores the dynamic optimization plot showing the optimum levels of the controlled variables that yield the highest % decolorizing, > 95%, in red-colored values. The inferred optimum conditions are catalyst type: 5400Aq, catalyst amount: 0.5 g, amount of peroxide, ≈ 2.0 mL of 3% H_2O_2, and pH: 2.

12 Preliminary Testing of Catalytic Activity Kinetics

The catalytic activity of the fabricated catalyst was tested axiomatically at the optimum conditions derived from the multilevel factorial experimental set for mining the kinetics-related information of the process. In the case of the 5400Aq catalyst, the semi-complete discoloration was achieved within fifteen minutes. The MO dye concentration decays exponentially, suggesting pseudo-first-order kinetics with respect to the MO azo dye concentration according to the equation $C = A\ \exp(-\ kt)$, where C is the concentration of the pollutant, k is the specific velocity in minutes^{-1}, t is the

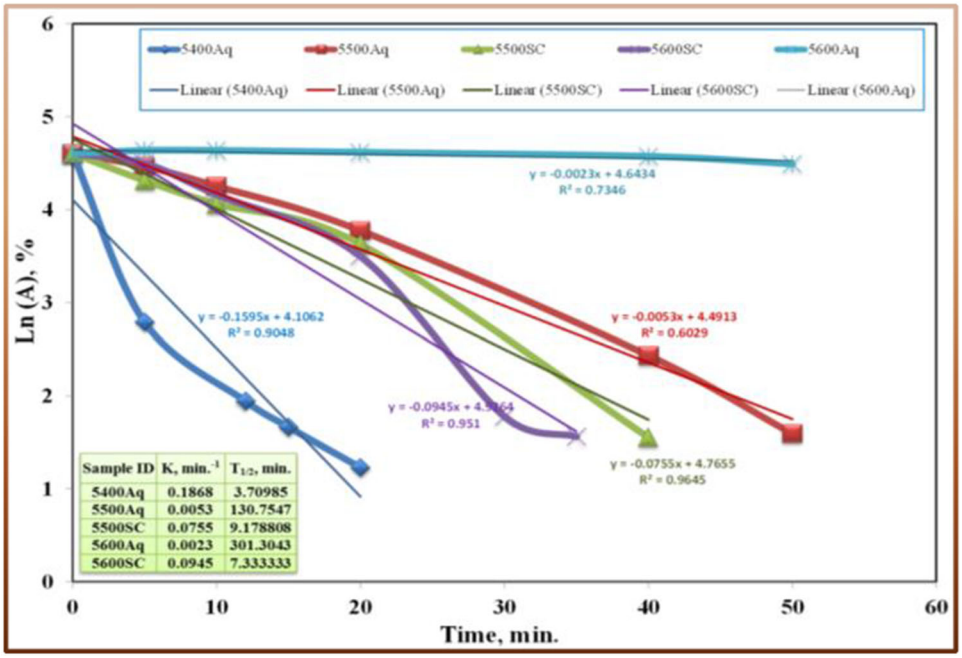

Fig. 15 Kinetics of the preliminary results of the decolorizing activity of the fabricated catalysts for methyl orange dye solution with 20 mg /L concentration. Conditions: 0. 5 g catalyst; sample volume: 50 mL; concentration: 10 mg-C/L; pH: 2; 2.5mL 3% H_2O_2; No irradiation; and continuous stirring at room temperature

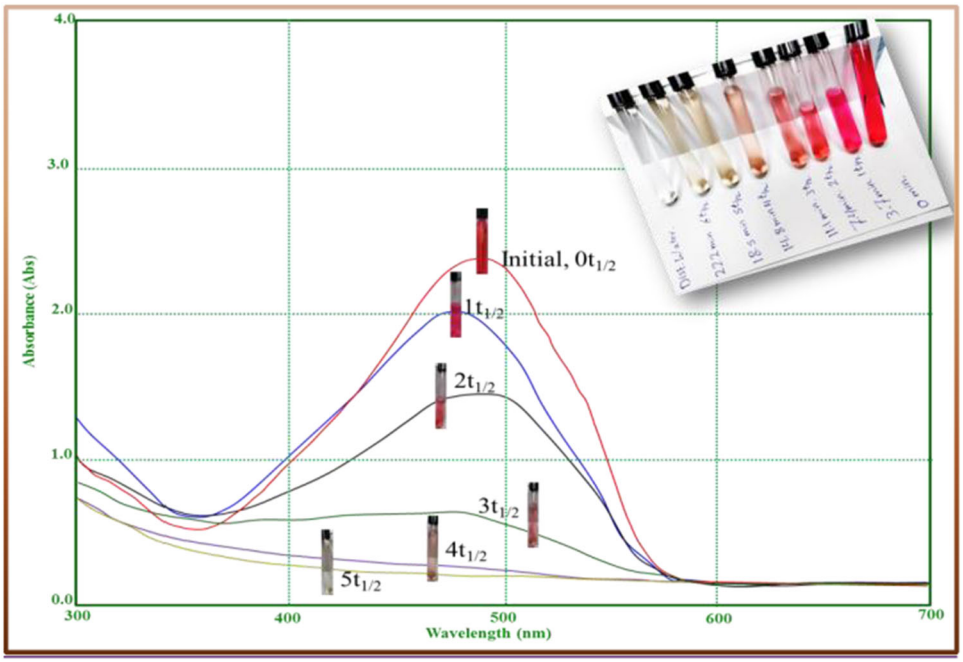

Fig. 16 Absorption spectra and the photographic pictures of the methyl orange dye degradation for five consecutive periods of half-live (≈ 3.7 min.) for 5400Aq catalyst. Conditions: 0. 5 g catalyst; sample volume: 50 mL; concentration: 10 mg-C/L; pH: 2; 2.5mL 3% H_2O_2; No irradiation; and continuous stirring at room temperature

time in minutes, where *C* is the concentration, and A is a constant. The rate constants and the respective half-life time of the process were driven for the materials tested and shown as intersect in Fig. 15. The reaction rate was far higher for 5400Aq with respect to the other catalyst types. The half-lives estimated were 3.7, 130, 9.18, 301.3, and 7.33 min for 5400Aq, 5500Aq, 5500SC, 5600Aq, and 5600SC, respectively. Time series absorption spectra of the dye degradation at five consecutive half-lives and the respective photographic pictures are shown in Fig. 16. As shown, the principal peak maxima gradually diminish until they disappear entirely after five consecutive periods of half-lives. This theme corroborates the suggestion of the pseudo-first-order kinetics of the process. Some discrepancies exist, necessitating a more controlled and well-optimized investigation. However, the results are so promising since complete decolorizing in the case of 5400Aq achieved in 15 min represents the shortest period reported so far in the literature, such as 60 min [70], 5 h [49], 100 min [46], and 4 h [82].

13 Conclusions

In this work, a simple, rapid, suitable for mass production, low-priced, facile, and single-step method for immobilizing CuO catalyst on sand support has been developed. The features of the immobilized catalyst-coating fabricated at different combustion temperatures and cooling rates were characterized using PXRD, SEM, and BET analysis. The PXRD spectra were deconvoluted and analyzed following the Rietveld refinement to extract the structural and crystallographic features of the catalytic coatings produced, confirming that the catalyst-coating is composed of one phase, Tenorite (CuO). The SEM confirmed that the coating has uniform spherical particle sizes in the submicron range (400–600 nm), which is consistently larger than the free powder prepared at the same conditions. Statistical analysis of the Rietveld refinement-derived data was conducted to figure out the optimum conditions, which were found to be 500 °C AT and the slow cooling rate. The optimum synthesis conditions inferred through the statistical analysis are: AT ≈ 400 °C and CR: SC. The fabricated material has demonstrated promising and superior catalytic activity performance for removing organic pollutants from aqueous solutions using hydrogen peroxide as an oxidant. The dynamic optimization plot helped infer the optimum conditions yielding the highest % decolorizing, > 95%, as catalyst type: 5400Aq (AT: 400 °C, CR: Aq, $CuAc_2.H_2O$/sand: 5:20), catalysts amount: 0.5 g, amount of peroxide, ≈ 2.0 mL of 3% H_2O_2, and pH: 2. The MO dye concentration decays exponentially according to pseudo-first-order kinetics with a half-life time of 3.7 min in case of 5400Aq. The results suggest that the fabricated CuO-coated sand is an effective and commercially viable catalyst, demonstrating the advantages of being simple, cost-effective, reliable, readily applicable and separable, efficient, of enhanced process kinetic, and needs no irradiation (i.e., low power consumption). The fabricated material is deemed a commercially viable catalyst for oxidizing the azo dyes in water effluents to meet the treatment standards, especially for small and medium units requiring simplified fixed installations and medium-skilled labor.

Acknowledgements The authors extend their appreciation to the deanship of scientific research at Shaqra University for funding this research work through project number (SU-ANN-202219).

Author Contributions Conceptualization was contributed by HEG, AAA, and FAG. Methodology was contributed by HEG, AAA, and FAG. Software was contributed by HEG. Validation was contributed by AAA and HEG. Formal analysis was contributed by HEG, and FAG. Investigation was contributed by HEG, and FAG. Resources were contributed by AAA, and HEG. Data curation was contributed by HEG, and FAG. Writing—original draft preparation, was contributed by HEG, and FAG. Writing—review and editing, was contributed by HEG, and FAG. Visualization was contributed by HEG, and FAG. Supervision was contributed by HEG. Project administration was contributed by AAA. Funding acquisition was contributed by AAA. All authors have read and agreed to the published version of the manuscript.

Funding The funding was provided by the Deanship of Scientific Research at Shaqra University through project number (SU-ANN-202219).

Data Availability The data presented in this study are available upon request from the corresponding author.

Declarations

Conflict of interest The authors declare that they have no known competing financial interests or personal relationships that could have appeared to influence the work reported in this paper.

References

1. United Nations, International Decade for Action "Water for Life" 2005–2015. Focus Areas: Water and sustainable development, (2015). https://www.un.org/waterforlifedecade/water_and_sustainable_development.shtml. Accessed 14 Nov 2022
2. Stefan, M.I.: Advanced oxidation processes for water treatment—fundamentals and applications (2017). https://doi.org/10.2166/9781780407197
3. Pires, C.A.; dos Santos, A.C.C.; Jordão, E.: Oxidation of phenol in aqueous solution with copper oxide catalysts supported on γ -Al_2O_3, pillared clay and TiO_2: comparison of the performance and costs associated with each catalyst. Braz. J. Chem. Eng. **32**, 837–848 (2015). https://doi.org/10.1590/0104-6632.20150324s00002232
4. SDWA, The Safe Drinking Water Act of 1996, U.S. Gov. Print. Off. (2000) 128
5. Saratale, R.G.; Ghodake, G.S.; Shinde, S.K.; Cho, S.K.; Saratale, G.D.; Pugazhendhi, A.; Bharagava, R.N.: Photocatalytic activity of CuO/$Cu(OH)_2$ nanostructures in the degradation of Reactive Green 19A and textile effluent, phytotoxicity studies and their biogenic properties (antibacterial and anticancer). J. Environ. Manag. **223**, 1086–1097 (2018). https://doi.org/10.1016/j.jenvman.2018.04.072
6. Saratale, R.G.; Saratale, G.D.; Chang, J.S.; Govindwar, S.P.: Decolorization and biodegradation of textile dye Navy blue HER by Trichosporon beigelii NCIM-3326. J. Hazard. Mater. **166**, 1421–1428 (2009). https://doi.org/10.1016/j.jhazmat.2008.12.068
7. Bedekar, P.A.; Saratale, R.G.; Saratale, G.D.; Govindwar, S.P.: Oxidative stress response in dye degrading bacterium Lysinibacillus sp. RGS exposed to Reactive Orange 16, degradation of RO16 and evaluation of toxicity. Environ. Sci. Pollut. Res. **21**, 11075–11085 (2014). https://doi.org/10.1007/s11356-014-3041-2
8. Saratale, R.G.; Saratale, G.D.; Chang, J.S.; Govindwar, S.P.: Bacterial decolorization and degradation of azo dyes: a review. J. Taiwan Inst. Chem. Eng. **42**, 138–157 (2011). https://doi.org/10.1016/j.jtice.2010.06.006
9. Sapkal, R.T.; Shinde, S.S.; Mahadik, M.A.; Mohite, V.S.; Waghmode, T.R.; Govindwar, S.P.; Rajpure, K.Y.; Bhosale, C.H.: Photoelectrocatalytic decolorization and degradation of textile effluent using ZnO thin films. J. Photochem. Photobiol. B Biol. **114**, 102–107 (2012). https://doi.org/10.1016/j.jphotobiol.2012.05.016
10. Salehi, K.; Bahmani, A.; Shahmoradi, B.; Pordel, M.A.; Kohzadi, S.; Gong, Y.; Guo, H.; Shivaraju, H.P.; Rezaee, R.; Pawar, R.R.; Lee, S.-M.: Response surface methodology (RSM) optimization approach for degradation of Direct Blue 71 dye using CuO–ZnO

nanocomposite. Int. J. Environ. Sci. Technol. **14**, 2067–2076 (2017). https://doi.org/10.1007/s13762-017-1308-0
11. Novotný, Č; Svobodová, K.; Benada, O.; Kofroňová, O.; Heissenberger, A.; Fuchs, W.: Potential of combined fungal and bacterial treatment for color removal in textile wastewater. Bioresour. Technol. **102**, 879–888 (2011). https://doi.org/10.1016/j.biortech.2010.09.014
12. Hu, E.; Wu, X.; Shang, S.; Tao, X.M.; Jiang, S.X.; Gan, L.: Catalytic ozonation of simulated textile dyeing wastewater using mesoporous carbon aerogel supported copper oxide catalyst. J. Clean. Prod. **112**, 4710–4718 (2016). https://doi.org/10.1016/j.jclepro.2015.06.127
13. Malatji, N.; Makhado, E.; Modibane, K.D.; Ramohlola, K.E.; Maponya, T.C.; Monama, G.R.; Hato, M.J.: Removal of methylene blue from wastewater using hydrogel nanocomposites: a review. Nanomater. Nanotechnol. **11**, 1–27 (2021). https://doi.org/10.1177/18479804211039425
14. Chemingui, H.; Rezma, S.; Lafi, R.; Alhalili, Z.; Missaoui, T.; Harbi, I.; Smiri, M.; Hafiane, A.: Investigation of methylene blue adsorption from aqueous solution onto ZnO nanoparticles: equilibrium and Box-Behnken optimisation design. Int. J. Environ. Anal. Chem. **00**, 1–26 (2021). https://doi.org/10.1080/03067319.2021.1897121
15. Samsami, S.; Mohamadi, M.; Sarrafzadeh, M.H.; Rene, E.R.; Firoozbahr, M.: Recent advances in the treatment of dye-containing wastewater from textile industries: overview and perspectives. Process Saf. Environ. Prot. **143**, 138–163 (2020). https://doi.org/10.1016/j.psep.2020.05.034
16. dos Santos, A.B.; de Madrid, M.P.; de Bok, F.A.M.; Stams, A.J.M.; van Lier, J.B.; Cervantes, F.J.: The contribution of fermentative bacteria and methanogenic archaea to azo dye reduction by a thermophilic anaerobic consortium. Enzyme Microb. Technol. **39**, 38–46 (2006). https://doi.org/10.1016/J.ENZMICTEC.2005.09.003
17. Matzek, L.W.; Carter, K.E.: Activated persulfate for organic chemical degradation: a review. Chemosphere **151**, 178–188 (2016). https://doi.org/10.1016/j.chemosphere.2016.02.055
18. Mahata, P.; Aarthi, T.; Madras, G.; Natarajan, S.: Photocatalytic degradation of dyes and organics with nanosized $GdCoO_3$. J. Phys. Chem. C. **111**, 1665–1674 (2007). https://doi.org/10.1021/jp066302q
19. Reza, K.M.; Kurny, A.; Gulshan, F.: Parameters affecting the photocatalytic degradation of dyes using TiO_2: a review. Appl. Water Sci. **7**, 1569–1578 (2017). https://doi.org/10.1007/s13201-015-0367-y
20. Kanakaraju, D.; Bin Ya, M.H.; Lim, Y.C.; Pace, A.: Combined adsorption/photocatalytic dye removal by copper-titania-fly ash composite. Surfaces and Interfaces **19**, 100534 (2020). https://doi.org/10.1016/j.surfin.2020.100534
21. Çifçi, D.I.; Terzi, S.; Meriç, S.: 7 -photocatalytic decolorization of two remazol dyes using TiO_2 impregnated pumice composite as catalyst. Nanotechnol. Water Wastewater Treat. Theory Appl. (2018). https://doi.org/10.1016/B978-0-12-813902-8.00007-1
22. Prasad, C.; Tang, H.; Liu, Q.Q.; Zulfiqar, S.; Shah, S.; Bahadur, I.: An overview of semiconductors/layered double hydroxides composites: Properties, synthesis, photocatalytic and photoelectrochemical applications. J. Mol. Liq. **289**, 2019 (2019). https://doi.org/10.1016/j.molliq.2019.111114
23. Saha, T.K.; Frauendorf, H.; John, M.; Dechert, S.; Meyer, F.: Efficient oxidative degradation of azo dyes by a water-soluble manganese porphyrin catalyst. ChemCatChem **5**, 796–805 (2013). https://doi.org/10.1002/cctc.201200475
24. Glaze, W.H.; Kang, J.W.; Chapin, D.H.: The chemistry of water treatment processes involving ozone, hydrogen peroxide and ultraviolet radiation. Ozone Sci. Eng. **9**, 335–352 (1987). https://doi.org/10.1080/01919518708552148
25. Bolton, J.R.; Bircher, K.G.; Tumas, W.; Tolman, C.A.: Figures-of-merit for the technical development and application of advanced oxidation technologies for both electric- and solar-driven systems. Pure Appl. Chem. **73**, 627–637 (2001). https://doi.org/10.1351/pac200173040627
26. Zhao, F.; Liu, Y.; Ben Hammouda, S.; Doshi, B.; Guijarro, N.; Min, X.; Tang, C.J.; Sillanpää, M.; Sivula, K.; Wang, S.: MIL-101(Fe)/g-C3N4 for enhanced visible-light-driven photocatalysis toward simultaneous reduction of Cr(VI) and oxidation of bisphenol A in aqueous media. Appl. Catal. B Environ. **272**, 119033 (2020). https://doi.org/10.1016/j.apcatb.2020.119033
27. Augugliaro, V.; Palmisano, G.; Palmisano, L.; Soria, J.: Heterogeneous photocatalysis and catalysis: an overview of their distinctive features. Elsevier, Amsterdam (2019) https://doi.org/10.1016/B978-0-444-64015-4.00001-8
28. Long, Z.; Li, Q.; Wei, T.; Zhang, G.; Ren, Z.: Historical development and prospects of photocatalysts for pollutant removal in water. J. Hazard. Mater. **395**, 122599 (2020). https://doi.org/10.1016/j.jhazmat.2020.122599
29. Montoya, J.F.; Velásquez, J.A.; Salvador, P.: The direct-indirect kinetic model in photocatalysis: a reanalysis of phenol and formic acid degradation rate dependence on photon flow and concentration in TiO_2 aqueous dispersions. Appl. Catal. B Environ. **88**, 50–58 (2009). https://doi.org/10.1016/j.apcatb.2008.09.035
30. Bajorowicz, B.; Kobylański, M.P.; Malankowska, A.; Mazierski, P.; Nadolna, J.; Pieczyńska, A.; Zaleska-Medynska, A.: Application of metal oxide-based photocatalysis (2018). https://doi.org/10.1016/B978-0-12-811634-0.00004-4
31. Loddo, V.; Roda, G.C.: Parrino Kinetic Aspects of Heterogeneous Catalytic Versus Photocatalytic Reactions. Elsevier, Amsterdam (2019) https://doi.org/10.1016/B978-0-444-64015-4.00007-9
32. Grabowska, E.; Marchelek, M.; Paszkiewicz-Gawron, M.; Zaleska-Medynska, A.: Metal Oxide Photocatalysts. Elsevier, Amsterdam (2018) https://doi.org/10.1016/B978-0-12-811634-0.00003-2
33. Omri, A.; Hamza, W.; Benzina, M.: Copyright. Appl. Catal. B Environ. **7**, 1–10 (2018). https://doi.org/10.1021/acs.est.6b02067
34. Manirul, S.; Sumantra, I.: Oxidation of organic compounds by hydrogen peroxide using polymer-anchored azo-metal catalysts 7–14 (2013). https://doi.org/10.1007/s11243-012-9654-8
35. Islam, S.M.; Paul, S.; Mobarok, M.; Roy, A.S.; Mondal, P.: Oxidation of organic compounds by hydrogen peroxide using polymer-anchored azo-metal catalysts. Transit. Met. Chem. **38**, 7–14 (2013). https://doi.org/10.1007/s11243-012-9654-8
36. Pirsaheb, M.; Hossaini, H.; Azizi, N.: Synthesized Cr/TiO_2 immobilized on pumice powder for photochemical degradation of acid orange-7 dye under UV/visible light: influential operating factors, optimization, and modeling. J. Environ. Health Sci. Eng. **18**, 1329–1341 (2020)
37. Chen, C.H.; Shieh, J.; Liao, H.Y.; Shyue, J.J.: Construction of titania-ceria nanostructured composites with tailored heterojunction for photocurrent enhancement. J. Eur. Ceram. Soc. **34**, 1523–1535 (2014). https://doi.org/10.1016/j.jeurceramsoc.2013.12.019
38. Bielan, Z.; Kowalska, E.; Dudziak, S.; Wang, K.; Ohtani, B.; Zielińska-Jurek, A.: Mono- and bimetallic (Pt/Cu) titanium(IV) oxide core–shell photocatalysts with UV/Vis light activity and magnetic separability. Catal. Today. **361**, 198–209 (2021). https://doi.org/10.1016/j.cattod.2020.05.034
39. Karlsson, H.L.; Cronholm, P.; Gustafsson, J.; Möller, L.: Copper oxide nanoparticles are highly toxic: a comparison between metal oxide nanoparticles and carbon nanotubes. Chem. Res. Toxicol. **21**, 1726–1732 (2008). https://doi.org/10.1021/tx800064j
40. Derikvandi, H.; Nezamzadeh-Ejhieh, A.: Increased photocatalytic activity of NiO and ZnO in photodegradation of a model drug aqueous solution: effect of coupling, supporting, particles size and

calcination temperature. J. Hazard. Mater. **321**, 629–638 (2017). https://doi.org/10.1016/j.jhazmat.2016.09.056
41. Bradu, C.; Frunza, L.; Mihalche, N.; Avramescu, S.M.; Neaţă, M.; Udrea, I.: Removal of reactive black 5 azo dye from aqueous solutions by catalytic oxidation using CuO/Al_2O_3 and NiO/Al_2O_3. Appl. Catal. B Environ. **96**, 548–556 (2010). https://doi.org/10.1016/j.apcatb.2010.03.019
42. Mahmood, T.; Saddique, M.T.; Naeem, A.; Westerhoff, P.; Mustafa, S.; Alum, A.: Comparison of different methods for the point of zero charge determination of NiO. Ind. Eng. Chem. Res. **50**, 10017–10023 (2011). https://doi.org/10.1021/ie200271d
43. Ethiraj, A.S.; Uttam, P.; Varunkumar, K.; Chong, K.F.; Ali, G.A.M.: Photocatalytic performance of a novel semiconductor nanocatalyst: copper doped nickel oxide for phenol degradation. Mater. Chem. Phys. **242**, 122520 (2020). https://doi.org/10.1016/j.matchemphys.2019.122520
44. Hermanek, M.; Zboril, R.; Medrik, I.; Pechousek, J.; Gregor, C.: Catalytic efficiency of iron(III) oxides in decomposition of hydrogen peroxide: competition between the surface area and crystallinity of nanoparticles. J. Am. Chem. Soc. **129**, 10929–10936 (2007). https://doi.org/10.1021/ja072918x
45. Azimi, S.; Nezamzadeh-Ejhieh, A.: Enhanced activity of clinoptilolite-supported hybridized PbS-CdS semiconductors for the photocatalytic degradation of a mixture of tetracycline and cephalexin aqueous solution. J. Mol. Catal. A Chem. **408**, 152–160 (2015). https://doi.org/10.1016/j.molcata.2015.07.017
46. Habibi, M.H.; Rahmati, M.H.: The effect of operational parameters on the photocatalytic degradation of Congo red organic dye using ZnO-CdS core-shell nano-structure coated on glass by Doctor Blade method. Spectrochim. Acta Part A Mol. Biomol. Spectrosc. **137**, 160–164 (2015). https://doi.org/10.1016/j.saa.2014.08.110
47. Munir, T.; Munir, H.S.; Kashif, M.; Fakhar-E-Alam, M.; Shahzad, A.; Amin, N.; Sajid, A.; Umair, M.: Synthesis and characterization of Copper Oxide nanoparticles by solution evaporation method. J. Optoelectron. Adv. Mater. **19**, 417–423 (2017)
48. Marabelli, F.; Parravicini, G.B.; Salghetti-Drioli, F.: Optical gap of CuO. Phys. Rev. B. **52**, 1433–1436 (1995). https://doi.org/10.1103/PhysRevB.52.1433
49. Ben-Moshe, T.; Dror, I.; Berkowitz, B.: Oxidation of organic pollutants in aqueous solutions by nanosized copper oxide catalysts. Appl. Catal. B Environ. **85**, 207–211 (2009). https://doi.org/10.1016/j.apcatb.2008.07.020
50. Dörner, L.; Cancellieri, C.; Rheingans, B.; Walter, M.; Kägi, R.; Schmutz, P.; Kovalenko, M.V.; Jeurgens, L.P.H.: Cost-effective sol-gel synthesis of porous CuO nanoparticle aggregates with tunable specific surface area. Sci. Rep. **9**, 1–13 (2019). https://doi.org/10.1038/s41598-019-48020-8
51. Du, X.; Zhang, Y.; Si, F.; Yao, C.; Du, M.; Hussain, I.; Kim, H.; Huang, S.; Lin, Z.; Hayat, W.: Persulfate non-radical activation by nano-CuO for efficient removal of chlorinated organic compounds: reduced graphene oxide-assisted and CuO (0 0 1) facet-dependent. Chem. Eng. J. **356**, 178–189 (2019). https://doi.org/10.1016/j.cej.2018.08.216
52. Alhalili, Z.: Green synthesis of copper oxide nanoparticles CuO NPs from eucalyptus globoulus leaf extract: adsorption and design of experiments. Arab. J. Chem. (2022). https://doi.org/10.1016/j.arabjc.2022.103739
53. Ben-Moshe, T.; Dror, I.; Berkowitz, B.: Copper oxide nanoparticle-coated quartz sand as a catalyst for degradation of an organic dye in water. Water. Air. Soil Pollut. **223**, 3105–3115 (2012). https://doi.org/10.1007/s11270-012-1093-9
54. Mazurkow, J.M.; Yüzbasi, N.S.; Domagala, K.W.; Pfeiffer, S.; Kata, D.; Graule, T.: Nano-sized copper (oxide) on alumina granules for water filtration: effect of copper oxidation state on virus removal performance. Environ. Sci. Technol. **54**, 1214–1222 (2020). https://doi.org/10.1021/acs.est.9b05211
55. Batista, A.P.L.; Carvalho, H.W.P.; Luz, G.H.P.; Martins, P.F.Q.; Gonçalves, M.; Oliveira, L.C.A.: Preparation of CuO/SiO_2 and photocatalytic activity by degradation of methylene blue. Environ. Chem. Lett. **8**, 63–67 (2010). https://doi.org/10.1007/s10311-008-0192-8
56. Li, H.; Zhu, J.; Xiao, P.; Zhan, Y.; Lv, K.; Wu, L.; Li, M.: On the mechanism of oxidative degradation of rhodamine B over $LaFeO_3$ catalysts supported on silica materials: role of support. Microporous Mesoporous Mater. **221**, 159–166 (2015). https://doi.org/10.1016/j.micromeso.2015.09.034
57. Valkaj, K.; Wittine, O.; Margeta, K.; Granato, T.; Katović, A.; Zrnčević, S.: Phenol oxidation with hydrogen peroxide using Cu/ZSM5 and Cu/Y5 catalysts, Polish. J Chem. Technol. **13**, 28–36 (2011). https://doi.org/10.2478/v10026-011-0033-6
58. Kalidhasan, S.; Dror, I.; Berkowitz, B.: Atrazine degradation through PEI-copper nanoparticles deposited onto montmorillonite and sand. Sci. Rep. **7**, 1–13 (2017). https://doi.org/10.1038/s41598-017-01429-5
59. Shao, L.; Liu, H.; Zeng, W.; Zhou, C.; Li, D.; Wang, L.; Lan, Y.; Xu, F.; Liu, G.: Immobilized and photocatalytic performances of PDMS-SiO_2-chitosan@TiO_2 composites on pumice under simulated sunlight irradiation. Appl. Surf. Sci. **478**, 1017–1026 (2019). https://doi.org/10.1016/j.apsusc.2019.02.060
60. Tavasol, F.; Tabatabaie, T.; Ramavandi, B.; Amiri, F.: Design a new photocatalyst of sea sediment/titanate to remove cephalexin antibiotic from aqueous media in the presence of sonication/ultraviolet/hydrogen peroxide: pathway and mechanism for degradation. Ultrason. Sonochem. **65**, 105062 (2020). https://doi.org/10.1016/j.ultsonch.2020.105062
61. Gosu, V.; Sikarwar, P.; Subbaramaiah, V.: Mineralization of pyridine by CWPO process using nFe0/GAC catalyst. J. Environ. Chem. Eng. **6**, 1000–1007 (2018). https://doi.org/10.1016/j.jece.2018.01.017
62. Huang, C.P.; Huang, Y.H.: Comparison of catalytic decomposition of hydrogen peroxide and catalytic degradation of phenol by immobilized iron oxides. Appl. Catal. A Gen. **346**, 140–148 (2008). https://doi.org/10.1016/j.apcata.2008.05.017
63. Hoefelmeyer, J.D.: Surface-Modified Anisotropic TiO_2 Nanocrystals Immobilized in Membranes: a Biologically Inspired Solar Fuel Catalyst. Elsevier, Amsterdam (2013) https://doi.org/10.1016/B978-0-444-53872-7.00012-1
64. Garrido-Ramírez, E.G.; Theng, B.K.G.; Mora, M.L.: Clays and oxide minerals as catalysts and nanocatalysts in Fenton-like reactions—a review. Appl. Clay Sci. **47**, 182–192 (2010). https://doi.org/10.1016/j.clay.2009.11.044
65. Taran, O.P.; Zagoruiko, A.N.; Yashnik, S.A.; Ayusheev, A.B.; Pestunov, A.V.; Prosvirin, I.P.; Prihod'Ko, R.V.; Goncharuk, V.V.; Parmon, V.N.: Wet peroxide oxidation of phenol over carbon/zeolite catalysts. Kinetics and diffusion study in batch and flow reactors. J. Environ. Chem. Eng. **6**, 2551–2560 (2018). https://doi.org/10.1016/j.jece.2018.03.017
66. Wan, J.; Zhao, F.; Meng, Y.; Guo, M.; Tang, C.; Shi, Y.; Ke, Y.; Hu, R.: Three-dimensional electrochemical degradation of p-aminophenol with efficient honeycomb block AC@Ti-Cu-Ni-Zn-Sb-Mn particle electrodes. Sep. Purif. Technol. **267**, 118662 (2021). https://doi.org/10.1016/j.seppur.2021.118662
67. El-Sheikh, A.H.; Al-Degs, Y.S.; Newman, A.P.; Lynch, D.E.: Oxidized activated carbon as support for titanium dioxide in UV-assisted degradation of 3-chlorophenol. Sep. Purif. Technol. **54**, 117–123 (2007). https://doi.org/10.1016/j.seppur.2006.08.020
68. Tsoncheva, T.; Genova, I.; Stoyanova, M.; Pohl, M.M.; Nickolov, R.; Dimitrov, M.; Sarcadi-Priboczki, E.; Mihaylov, M.; Kovacheva, D.; Hadjiivanov, K.: Effect of mesoporous silica topology on the formation of active sites in copper supported catalysts for methanol decomposition. Appl. Catal. B Environ. **147**, 684–697 (2014). https://doi.org/10.1016/j.apcatb.2013.10.002

69. Kitis, M.; Karakaya, E.; Yigit, N.O.; Civelekoglu, G.; Akcil, A.: Heterogeneous catalytic degradation of cyanide using copper-impregnated pumice and hydrogen peroxide. Water Res. **39**, 1652–1662 (2005). https://doi.org/10.1016/j.watres.2005.01.027
70. Omri, A.; Hamza, W.; Benzina, M.: Photo-fenton oxidation and mineralization of methyl orange using Fe-sand as effective heterogeneous catalyst. J. Photochem. Photobiol. A Chem. **393**, 112444 (2020). https://doi.org/10.1016/j.jphotochem.2020.112444
71. Yip, A.C.K.; Lam, F.L.Y.; Hu, X.: Chemical-vapor-deposited copper on acid-activated bentonite clay as an applicable heterogeneous catalyst for the photo-fenton-like oxidation of textile organic pollutants. Ind. Eng. Chem. Res. **44**, 7983–7990 (2005). https://doi.org/10.1021/ie050647y
72. Liu, F.; Zhang, H.; Yan, Y.; Huang, H.: Graphene as efficient and robust catalysts for catalytic wet peroxide oxidation of phenol in a continuous fixed-bed reactor. Sci. Total Environ. **701**, 134772 (2020). https://doi.org/10.1016/j.scitotenv.2019.134772
73. Bellini, J.V.; Machado, R.; Morelli, M.R.; Kiminami, R.H.G.A.: Thermal, structural and morphological characterisation of freeze-dried copper(II) acetate monohydrate and its solid decomposition products. Mater. Res. **5**, 453–457 (2002). https://doi.org/10.1590/s1516-14392002000400010
74. Lin, Z.; Han, D.; Li, S.: Study on thermal decomposition of copper(II) acetate monohydrate in air. J. Therm. Anal. Calorim. **107**, 471–475 (2012). https://doi.org/10.1007/s10973-011-1454-4
75. Barakat, N.A.M.; Yassin, M.A.; Al-Mubaddel, F.S.; Amen, M.T.: New electrooxidation characteristic for Ni-based electrodes for wide application in methanol fuel cells. Appl. Catal. A Gen. **555**, 148–154 (2018). https://doi.org/10.1016/j.apcata.2018.02.016
76. Whiteoak, C.J.; Britovsek, G.J.P.; Gibson, V.C.; White, A.J.P.: Electronic effects in oxo transfer reactions catalysed by salan molybdenum(VI) cis-dioxo complexes. Dalt. Trans. (2009). https://doi.org/10.1039/b820754b
77. Naktiyok, J.; Özer, A.K.: Synthesis of copper oxidE (CuO) from thermal decomposition of copper acetate monohydrate ($Cu(CH_3COO)_2.H_2O$). Omer Halisdemir Univ. J. Eng. Sci. **8**, 1292–1298 (2019). https://doi.org/10.28948/ngumuh.598177
78. Runčevski, T.; Brown, C.M.: The rietveld refinement method: half of a century anniversary. Cryst. Growth Des. **21**, 4821–4822 (2021). https://doi.org/10.1021/acs.cgd.1c00854
79. Barthel, K.U.: 3D-Data Representation with ImageJ. In: ImageJ User and Developer Conference 2006, Luxembourg, pp. 1–4 (2006)
80. Pookmanee, P.; Sangthep, P.; Tafun, J.; Kruefu, V.; Kojinok, S.; Phanichphant, S.: Synthesis, characterization and its photocatalytic of copper oxide (Cuo) powder. Mater. Sci. Forum. MSF **962**, 70–76 (2019). https://doi.org/10.4028/www.scientific.net/MSF.962.70
81. Minitab® 18 Support, What are response surface designs, central composite designs, and Box-Behnken designs?, (n.d.).
82. Singh, L.; Rekha, P.; Chand, S.: Cu-impregnated zeolite Y as highly active and stable heterogeneous Fenton-like catalyst for degradation of Congo red dye. Sep. Purif. Technol. **170**, 321–336 (2016). https://doi.org/10.1016/j.seppur.2016.06.059